PURDUE UNIVERSITY
GRADUATE SCHOOL
Thesis/Dissertation Acceptance

This is to certify that the thesis/dissertation prepared

By Akshay Prabhu Verleker

Entitled
Monte Carlo Simulation to Study Propagation of Light through Biological Tissues

For the degree of   Master of Science in Biomedical Engineering

Is approved by the final examining committee:

Edward Berbari
_____
Chair

Keith Stantz

Ken Yoshida

To the best of my knowledge and as understood by the student in the *Research Integrity and Copyright Disclaimer (Graduate School Form 20)*, this thesis/dissertation adheres to the provisions of Purdue University's "Policy on Integrity in Research" and the use of copyrighted material.

Approved by Major Professor(s): Keith Stantz

_____

Approved by: Edward Berbari   9/15/2011
Head of the Graduate Program   Date

PURDUE UNIVERSITY
GRADUATE SCHOOL

Research Integrity and Copyright Disclaimer

Title of Thesis/Dissertation:

Monte Carlo Simulation to Study Propagation of Light through Biological Tissues

For the degree of _____Master of Science in Biomedical Engineering_____

I certify that in the preparation of this thesis, I have observed the provisions of *Purdue University Executive Memorandum No. C-22,* September 6, 1991, *Policy on Integrity in Research.**

Further, I certify that this work is free of plagiarism and all materials appearing in this thesis/dissertation have been properly quoted and attributed.

I certify that all copyrighted material incorporated into this thesis/dissertation is in compliance with the United States' copyright law and that I have received written permission from the copyright owners for my use of their work, which is beyond the scope of the law. I agree to indemnify and save harmless Purdue University from any and all claims that may be asserted or that may arise from any copyright violation.

Akshay Prabhu Verleker
_____
Printed Name and Signature of Candidate

9/15/2011
_____
Date (month/day/year)

MONTE CARLO SIMULATION TO STUDY PROPAGATION OF LIGHT

THROUGH BIOLOGICAL TISSUES

A Thesis

Submitted to the Faculty

of

Purdue University

by

Akshay Prabhu Verleker

In Partial Fulfillment of the

Requirements for the Degree

of

Master of Science in Biomedical Engineering

December 2011

Purdue University

Indianapolis, Indiana

ACKNOWLEDGEMENTS

I would like to sincerely thank my graduate advisor and mentor Dr. Keith Stantz for his assistance and guidance during my master's research in Photoacoustic Tomography in the Department of Imaging Sciences at Indiana University - Purdue University at Indianapolis. Dr. Stantz was generous in sharing his research experience with me and guided me during my work in his laboratory. His expertise in Photoacoustic Tomography and his constant contributions to my work has been a source inspiration for my work under him. As a mentor, he has always been motivating me to achieve better results and to understand the principles behind the science of photoacoustic imaging.

I would like to thank my advisory committee members Dr. Edward Berbari, Professor and Chairman of the Department of Biomedical Engineering at Purdue University, Indianapolis and Dr. Ken Yoshida, Assistant Professor of Biomedical Engineering, for their contribution to guiding me in successfully completing my graduate research.

I would also like to specially thank Michael Schaffer, graduate student and fellow researcher from the Department of Health Sciences at Purdue University for his guidance and support. Michael has always been a fellow guide and a mentor to me and has constantly shared his graduate research experience, which helped make this project a success. I would also like to thank Ning Cao, graduate student and coworker, department of Health Sciences for her support in my research.

I also thank Ms. Valerie Lim Diemer for helping me in formatting this thesis. Her guidance in planning my graduate studies has finally made my thesis possible.

TABLE OF CONTENTS

LIST OF TABLES

LIST OF FIGURES

ABSTRACT

Prabhu Verleker, Akshay. M.S.B.M.E., Purdue University, December 2011. Monte Carlo Simulation to Study Propagation of Light through Biological Tissues. Major Professor: Keith Stantz.

Photoacoustic Imaging is a non-invasive optical imaging modality used to image biological tissues. In this method, a pulsating laser illuminates a region of tissues to be imaged, which then generates an acoustic wave due to thermal volume expansion. This wave is then sensed using an acoustic sensor such as a piezoelectric transducer and the resultant signal is converted into an imaging using the back projection algorithm. Since different types of tissues have different photo-acoustic properties, this imaging modality can be used for imaging different types of tissues and bodily organ systems.

This study aims at quantifying the process of light conversion into the acoustic signal. Light travels through tissues and gets attenuated (scattered or absorbed) or reflected depending on the optical properties of the tissues. The process of light propagation through tissues is studied using Monte Carlo simulation software which predicts the propagation of light through tissues of various shapes and with different optical properties. This simulation gives the resultant energy distribution due to light absorption and scattering on a voxel by voxel basis.

The Monte Carlo code alone is not sufficient to validate the photon propagation. The success of the Monte Carlo code depends on accurate prediction of the optical properties of the tissues. It also depends on accurately depicting tissue boundaries and thus the resolution of the imaging space. Hence, a validation algorithm has been designed

so as to recover the optical properties of the tissues which are imaged and to successfully validate the simulation results. The accuracy of the validation code is studied for various optical properties and boundary conditions. The results are then compared and validated with real time images obtained from the photoacoustic scanner. The various parameters for the successful validation of Monte Carlo method are studied and presented.

This study is then validated using the algorithm to study the conversion of light to sound. Thus it is a significant step in the quantification of the photoacoustic effect so as to accurately predict tissue properties.

1. INTRODUCTION

1.1 Problem Statement

Recent advances in the field of optical imaging and photoacoustic tomography, for medical diagnosis, has created a need for quantification of the passage of light through biological tissues and the need to understand the acoustic response of materials. The use of optical/acoustic tissue phantoms and simulation modeling has provided insights into the theory of light propagation as well as challenged some of the old concepts in optics and acoustics. Various studies over the years have provided new inputs into the stochastic nature of light propagation and have resulted in the emergence of Monte Carlo simulation as a major tool for validation of optical studies.

The use of Monte Carlo simulation not only validates light transport, but can also be used as a means to understand the conversion of optical energy into acoustic energy. These methods provide a means of validating the photoacoustic effect and combined with the use of optical and acoustic phantoms, they provide a methodical approach to quantifying the data as produced by the photoacoustic scanner. The ultimate goal of such a study would be to recover the optical properties of the substance imaged, thereby deriving valuable inputs for medical diagnostic applications.

1.2 Photoacoustic Tomography (PCT)

Photoacoustic Imaging is an optical imaging technique used to image tissues. In this modality, a pulsated laser is used to illuminate the object, which causes localized heating and volume expansion and results in an acoustic wave. The high frequency acoustic signal is then sensed using array of ultrasound sensors. The image contrast is proportional

to the energy absorbed by the tissue being imaged. This imaging modality thus gives a fairly accurate representation of the optical properties of the tissues. The final image is obtained using a filtered back projection algorithm.

Since the PCT image depends on the absorption coefficient of the object, it has several advantages over other imaging methods (CT and MRI) such as good spatial resolution and direct visualization of the optical properties (absorption coefficient) of the object being imaged. It is also a safe imaging technique as it uses a non-ionizing, low power laser source and causes no harm to tissues. Most importantly functionalized and quantitative images can be obtained using PCT.

PCT is most commonly used in imaging hemoglobin levels in blood. This is because hemoglobin has different absorption properties for different wavelengths. Also the response of oxy and de-oxy hemoglobin is different at the same wavelength. This gives an accurate representation of the amount of oxy and de-oxy hemoglobin concentration in blood vessels. This provides PCT with a unique advantage for applications in tumor studies and as a functionalized imaging modality.

1.3 Review of Light Propagation through Biological Tissues

Optical imaging techniques for medical applications require a thorough understanding of the nature of light propagation through biological tissues. Photoacoustic tomography being dependent on laser light propagation and absorption relies on the optical properties of the tissues being imaged. A variety of models have been developed which predict the fluence, transmission and reflection of light in tissues. Most of these methods are approximations of the radiative transport theory such as the diffusion based theory[1]. Studies involving measurement of attenuation cum scattering coefficients, penetration depth, and anisotropy factors have been performed at different wavelengths for different biological tissues[1].

The transport theory deals with the propagation of laser light energy through tissues. It is considered to be more accurate as compared to Maxwell's equation since it takes into account the inhomogeneous nature of biological tissues[1]. The radiative transport Equation 1 is as follows:

$$s. \nabla L(r,s) = -(\mu a + \mu s)L(r,s) + \mu s \int_{4\pi} p(s, s1)L(r, s1)d \quad (1)$$

Where L(r,s) is the radiance of light travelling in direction s which is a unit vector. μa is the absorption coefficient while μs is the scattering coefficient. The addition of these two gives the total attenuation coefficient. Thus the above Equation 1 states that the radiance of light gets reduced with scattering and absorption and increases due to scattering from direction s1 into direction s. Also the trems dw refers to the solid angle in the direction of s1 and p(s,s1) refers to the phase function. The phase function refers to the scattering angle and can be characterized by the parameter g which is also known as the anisotropy factor and is the cosine average of the phase function.

The basic assumption of the radiative transport theory is that it assumes the scattering and absorbing particles to be homogeneously distributed within the medium. This along with the knowledge of the scattering and absorption coefficients gives the light distribution or fluence as well as absorbed energy within the medium. However in order to predict the above mentioned optical properties, we have to find a solution to the transport equation. This leads to several approximations depending on the type of irradiance and such as diffuse or collimated types as well as the optical boundary conditions1 which are in turn dependent on the indices of reflection. For a depth which is far from the source of light, two solutions have been derived to account for unscattered transmission and an asymptotic fluence-rate.

Unscattered transmission is explained using Beer's Law which is given as[1]:

$$T = e^{-\mu t} \quad (2)$$

Where t is the thickness and T is the transmission (unscattered) while μ refers to the total attenuation coefficient. This shows that the light is attenuated in an exponential manner through the bulk of the tissue. Consequently the fluence rate also decreases exponentially with the rate of decay proportional to the effective attenuation coefficient[1].

A further modification of the Beer's Law is made so as to account for scattered components as follows[1]:

$$L(r,s) = L_c(r,s) + L_d(r,s) \quad (3)$$

Where L_c is the light which has had no interaction with the tissues while L_d is the part which has undergone scattering. Thus using this diffuse theory approximation in the RTE equation, the fluence can be simplified to[1]:

$$\varphi(r) = \int_{4\pi} L_d(r,s)d\omega \quad (4)$$

The factors which affect the accuracy of the diffuse approximation are the anisotropy factor, the ratio of scattering-to-absorption coefficients and the depth of the tissue from the light source along with the boundaries[2]. The most commonly used phase function which is compatible with the diffusion equation is the Henyey- Greenstein function[3]. The delta-Eddington phase function which makes use of the Henyey-Greenstein scattering is found to be ideal for light propagation in tissues. This is done by the following substitutions[4]:

$$\frac{g_{HG}}{1+g_{HG}} = g \quad (5)$$

$$\mu_s(1 - g_{HG}^2) = \mu_s^1 \quad (6)$$

This gives the total fluence rate in a slab of finite depth as[4]:

$$\varphi(z) = a_1 \exp(kz) + a_2 \exp(-kz) + a_3 \exp(-\mu_t z) \quad (7)$$

Where z is the depth while k is approximately equal to μ_{eff}. This condition is valid only if the absorption coefficient is significantly lower than the scattering

coefficient. As per the diffusion theory the reflectance R and the transmittance T are given by[5,6,7,8]:

$$R = -\frac{\mu_s g}{\mu_a + (1-g)\mu_s} + h/2(a_1 k - a_2 k - a_3 k) \quad (8)$$

$$T = \frac{\mu_s g e^{-\mu_t t}}{\mu_a + (1-g)\mu_s} - (a_1 k e^{kt} - a_2 k e^{kt} - a_3 \mu_t e^{-\mu_t t}) \quad (9)$$

The total transmission is the sum of the transmission as shown by Equation 2 and the one shown by Equation 9. The measurement of total reflectance and transmission gives the three optical coefficients namely the absorption coefficient (μ_a), scattering coefficient (μ_s), and the anisotropy factor (g). The reduced scattering coefficient can be calculated by using the following equation [9, 10]:

$$\mu_s^1 = (1-g)\mu_s \quad (10)$$

However, when we consider tissues with mismatched boundaries and different optical properties, then the relation between reflectance, transmission and the three optical parameters become complicated and needs iterative methods to recover these properties. One of the most commonly used iterative methods is Monte Carlo simulation which can recover the optical properties of the media.

1.4 Monte Carlo Simulations

The first people to introduce Monte Carlo simulations into the area of laser propagation through tissues were Wilson and Adam [11, 12]. As per the definition given by Lux[13] : A Monte Carlo method involves the construction of a stochastic model where the physical quantity to be measured is equal to the expected value of a random variable. This is determined using multiple independent sampling of the random variable.

The current approach uses Monte Carlo simulation to simulate the propagation of light through tissues with certain optical properties and uses an iterative algorithm to calculate backwards the absorption coefficient of the object (e.g. tumor) being imaged.

The iterative recovery of the absorption coefficient also serves as a validation method for the Monte Carlo algorithm[14]. The accuracy and effectiveness of the Monte Carlo algorithm depends on the number of photons being simulated which determines the signal-to-noise ratio[14] and thus affects the efficiency of the iterative back-calculation of the absorption coefficient. With a sufficiently large number of photon packets, the Monte Carlo is seen to be a more effective method of optical property recovery as compared to the Diffusion theory. This comes at the cost of the simulation time due to the large number of iterations[15]. However the computation time could be minimized using better processing powers as available today. This project uses the GPU based CUDA software which utilizes the parallel processing power of the GPUs and thus reduces computation time as compared to the previous Monte Carlo versions which were based on serial processing using CPUs[16, 17, 18].

1.5 Parallel Processing using CUDA

Computation using parallel processing is always seen to enhance the speed of computation and reduce the processing time. Graphical Processing Units (GPUs) are made of multiple cores and hence, offer a massive increase in parallel computation capabilities as compared to Central Processing Units (CPUs) [16, 17, 18]. Even a low cost GPU gives more than a thousand times faster computation power as compared to a standard CPU which uses serial computation. Since photon migration problems use complex algorithms and can be adapted to several independent parallel computations, GPU processing can be applied for increasing the efficiency of the Monte Carlo simulations for photon transport through complex media.

Due to very low latency of memory, well optimized process pipelines and hierarchy based thread structure; GPUs provide a well optimized computing platform for parallel computation[16]. Since photon propagation is an independent phenomenon, use of parallel computation capabilities of the GPU has been well optimized and can reduce the computation times as compared to serial processing methods. This project utilizes the

GPU based Monte Carlo software as was developed by Dr Qianqian Fang and Dr David Boas which utilizes the parallel processing of Nvidia GPUs using the Compute Unified Device Architecture[16]. This code uses the several parallel random number generators to generate photon packets which travel through complex media which are denoted by a voxelated space. Thus complex shapes are created using by denoting specific voxels with optical properties to represent different media for photon propagation[14, 16].

<div align="center">1.6 <u>Recovery of Optical Properties</u></div>

The most important criteria for any successful simulation are its validation techniques. Similarly for the Monte Carlo algorithm to be declared as successful in simulating propagation of photons through complex tissue structures, it has to be able to accurately predict the optical coefficients of the object being imaged/ simulated. The recovery of the absorption and scattering coefficients, the anisotropy factor and the refraction coefficient are important in order to determine the optical properties of the tissue. Successful recovery would also prove the validity of the Radiative Transfer Equation and thus validate the photon transport method as simulated by the Monte Carlo method[14]. The recovery of all the three optical properties simultaneously not only requires accurate prediction of boundary conditions, but also requires very large computation times. Hence, prior knowledge of two out of three optical properties has been used by most researchers for validation purposes. Since the current Monte Carlo code is based on the energy absorbed per unit volume of the voxel space, recovery of the absorption coefficient for known values of scattering coefficient, anisotropy factor and the refraction coefficient are considered as appropriate method for this study.

In order to study the process of recovery of absorption coefficients, we need to understand the equations which allow us to do so. The Beer Lambert Law can be applied for a light of beam of incident intensity I_0 on a slab of thickness x. As shown in Equation 2 the light transmission (no units) is logarithmically dependent n the product of the

absorption coefficient per unit length (μunit) of the substance[16] and the path length x which is the thickness of the slab. This relation is shows as follows:

$$T = e^{-\mu_{unit}x} \quad (11)$$

The transmission (T) is also defined as the ratio of the light intensity of the beam (I_1) coming out of the slab to the light intensity (I_0) of the beam incident on the slab and is given by:

$$T = I_1/I_0 \quad (12)$$

From Equations 11 and 12 it can be determined that:

$$I_1 = I_0 \, e^{-\mu_{unit}x} \quad (13)$$

The amount of energy which has been absorbed by a substance is given by the relation:

$$E_{ab} = Vt(I_0 - I_1) \quad (14)$$

From Equations 13 and 14 and by using Taylor expansion for a small x, it can be derived that:

$$E_{ab} = VtI_0\mu_{unit}x = V\phi\mu_a \quad (15)$$

Where φ is the fluence and μ is the absorption coefficient. Thus the equation which would be used for the recovery of absorption coefficient becomes[16]:

$$\mu_a = E_{ab}/\phi \quad (16)$$

The units for the absorption coefficient are mm^{-1}.

Determining the optical properties give a direct indication of the physical and chemical composition of the tissue being imaged and hence, is used as a tool in diagnosis of cancer. Though simultaneous recovery of all the optical properties would be ideal, it would require enormous amounts of computation time and would need complex algorithms to determine the interdependence between the optical properties. Hence, the

recovery of absorption coefficient which directly affects the energy deposition within each voxel is considered and implemented, with known values of anisotropy factor, refraction coefficient and scattering coefficient. This improves the speed of recovery as well as accuracy of the computation results.

The use of the Equation 16 which relates between the absorption coefficient, the fluence and the energy absorbed, allows us to recover the absorption coefficient when the other two quantities, i.e., the energy absorbed and the fluence in the voxel are given. In order to determine these quantities for every voxel, the Monte Carlo has to be able to generate a voxelated map of the fluence and the energy maps. The current code which was used could generate the fluence profile for every voxel. So in order to recover the energy absorbed, the following relation was used as stated in Equation 16:

$$E_{ab} = \mu_a \phi \quad (29)$$

It is important at this point to note that the value of μa used here, is an arbitrary input value used for that particular iteration of the Monte Carlo program and recovers the fluence ϕ. In every such iteration the value of recovered μa is updated and becomes the new arbitrary value for the next run of the Monte Carlo simulation. Thus the updated value of μa becomes the input for the next simulation run which then outputs the fluence profile, and both these quantities (ϕ and μa) are used to recover the value of the energy absorbed.

The next problem is the updating of the absorption coefficient. This process requires a reference energy map which could be used to derive the new values of the absorption coefficient. It uses the relation in Equation 16 in the following form:

$$\mu_a^{k+1} = \widehat{H}/\phi^k \quad (30)$$

Here $\widehat{H}$ is a reference energy map, μ_a^{k+1} is the recovered absorption coefficient and ϕ^k is the fluence profile obtained for the iteration k. The value of μ_a^{k+1} becomes the input value for the next simulation run.

2. OBJECTIVES

This study is a continuation of the study done by Jye Cheong[14]. The Monte Carlo code used in the previous study involved smooth object boundaries and computation using serial processing. The Monte Carlo code used in this study involves voxelated space with rough edges along voxel boundaries. Also the computation here is done using parallel processing power of CUDA enabled Graphical Processing Units (GPUs) provided by Nvidia. The code used in this study has been originally developed by Dr Qianqian Fang[16] and has been modified to suit the needs of photoacoustic imaging scenario as well as with the optical properties of tumors found in breast cancer tissues.

2.1 Specific Aims

The goal is to remove the need to simulate an object based on predefined (mathematically defined) surface boundaries. The MC algorithm should be able to read a 3D image, where each voxel in this image has a unique μ_s, g, μ_a (note: n, the index of refraction, remains constant for all voxels).The main objectives of this study are as follows:

- SA1: Simulate and compare the absorption and photon fluence distribution for a sphere, an ellipse, and a heterogeneous object.
- SA2: Test convergence of the iterative MC photon correction algorithm using the new MC algorithm for objects in SA1, and for different levels of noise.

- SA3: Test convergence, accuracy, and precision of the MC photon correction algorithm for 3D FBP PCT images.

2.2 Methodology

As state earlier the Monte Carlo method involves statistical sampling of the events (photon-tissue interactions) which occur under local rules of propagation. The deflection angle for scattering event and the step-size for photon interaction is decided using probability distributions. In this method each photon is assumed to be having particle properties. The optical properties are assumed to be macroscopic and distributed uniformly over small unit volumes known as voxels. Since any statistical analysis requires a large number of sampling events, similarly the Monte Carlo simulation too requires large number photons to be simulated for successfully predicting the photon transport through complex media.

The code used is able to simulate objects with different shapes in a 3 dimensional voxelated space. The object boundaries are defined as per the dimensions of the object and it encompasses specific voxels as denoted by the Cartesian coordinate system used. The Cartesian coordinates are useful in denoting the 3D space and have been used to defines, object boundaries, position of the source as well as the domain boundaries. The direction of the light beam to be simulated is also designated in vector form using the Cartesian coordinate system.

The photons can be launched from any point within the observation space (three dimensional space) and travel in the direction as denoted by the vector coordinates. The photons interact with the voxels which lie in the path before travelling to the boundary of the observation space. Upon reaching the observation space boundary, one can either choose for the photons to exit the domain space or to be reflected back. Since the photoacoustic model uses water as the domain for tissue boundaries, we have chosen to allow the photons to be exited from the observation space at the domain boundary. In a

different study, the user can always allow the boundary reflections to take place depending on the imaging modality used.

The domain space is defined by 3 dimensional units called as voxels. The voxel is a cuboid of definite dimensions. The dimensions can be defined as needed by the user. In this study we have defined voxels with 1mm sides, thus having a volume of $1mm^3$. The voxel size affects the computation time of the code and also affects the smoothness of the object boundary. Larger the voxel size lesser is the computation time, while smaller voxel size implies larger computation times. However smaller voxel size results in smoother object boundaries and more accurate depiction of the object space and boundaries. This comes at a cost of the computation time. However using the Monte Carlo software on CUDA based parallel processing platform minimizes this disadvantage and allows us to increase the speed more than a thousand times as compared to serial processing techniques using traditional CPU based software. This is a major advantage of the current software as compared to the code used in the previous study[14, 16].

This study also modifies the existing code as developed by Fang et al[16], which used only a pencil shaped beam. Photoacoustic imaging systems use laser beams which have super-Gaussian beam profiles. Hence, in order to replicate and validate the imaging system we need to achieve a beam profile as close to the one used in the real present day systems. This study has modified the existing code to simulate a super-Gaussian beam profile which is similar to the beam as used in the machine developed by Optosonics Inc. This will allow for more accurate prediction of optical properties as those which have been determined from the PCT images.

3. MONTE CARLO SIMULATION

3.1 Algorithm and Flowchart

Figure 3.1 shows the flowchart of the Monte Carlo software. The random nature of light can be simulated successfully by assigning a random variable to the random quantity to be simulated. In this case the random variable is a number having a normal distribution and is used to determine the step size and the scattering direction of the propagating photon.
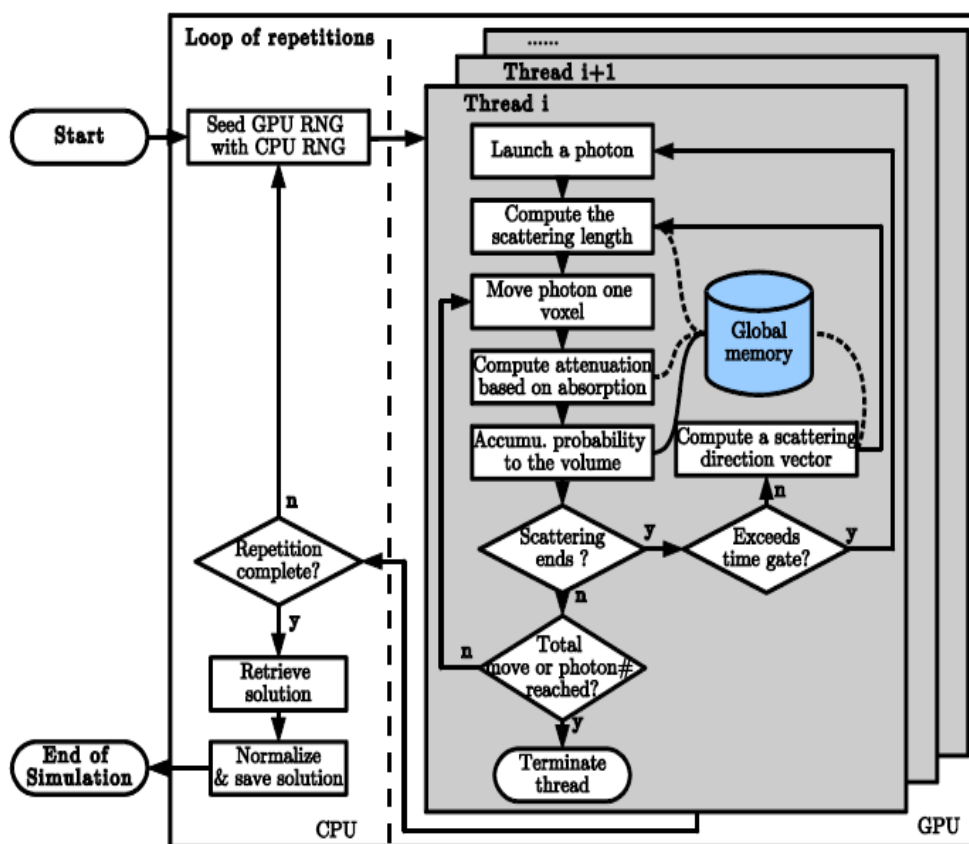
Figure 3.1 Monte Carlo algorithm for photon propagation[16]

3.1.1 Photon Packet Generation and Launch

The photons are generated based on random number generators which decide the angle of photon propagation, the step size and the scattering angle. The nature of random number generation is explained in several books[13, 19, 20]. The random number generated is normally distributed between 0 and 1 as mentioned by L. Wang. It is this number which is used to initialize the above parameters of photon propagation.

3.1.2 Photon Propagation, Absorption and Energy Deposition

For a voxel volume of ΔV, based on the conservation of energy equation[21] the raw probability which accumulates in the volume is given by:

$$F(\bar{r}, t) = \frac{P(\bar{r},t)E_a/E_t}{\sum_i \sum_j P(\bar{r}_\imath,t_j)\mu_a(\bar{r}_\imath)\Delta V \Delta t} \quad (17)$$

Where $P(\bar{r}, t)$ is the 'raw probability' and has no units, at position r and time t. The ratio of total energy which has been absorbed is given by Ea/Et in the time period or time-gate of Δt[16]. $F(\bar{r}, t)$ is the fluence (mm^{-2}s^{-1}) and µa is the absorption coefficient (mm-1).

The free path of a photon is derived from a random number generator. It is a number between 0 and 1 and is used to determine the photon step size which is given by the following function:

$$S1 = -\ln(\varepsilon)/\mu_t \quad (18)$$

Where S1 is the step size and ln(ε) is the free path obtained from the random number generator. The term µt stands for the transmission coefficient and is equal to the sum of the absorption and scattering coefficients given as:

$$\mu_t = \mu_a + \mu_s \quad (19)$$

It can be thus derived that the step size is dependent on the absorption and scattering coefficients and is thus different in different media. Hence, the Monte Carlo

code needs to compute the step size every time the photon enters a voxel having different optical properties as compared the previous voxel which the photon has exited.

The step size is updated along every axis using vector addition in the Cartesian coordinate system in order to determine and update the new location.

Once the photon travels along a distance equal to the step size, the interaction of the photon is determined at that spot known as the interaction site. At every such site, the photon is either scattered or absorbed. Accordingly the partial weight of the photon is reduced and the lost weight is then deposited in that particular voxel where the interaction occurs. The weight absorbed is given by:

$$\Delta w = w\left(\frac{\mu_a}{\mu_t}\right) \quad (20)$$

Here Δw is the weight lost by the photon whose initial weight 'w' now becomes w - Δw. Thus the ratio of weight lost by the photon is dependent on the ratio of the absorption coefficient to the total transmission coefficient. Thus while absorption property plays a direct role in the energy absorbed by the medium the scattering coefficient also influences the total transmission coefficient and is affects the energy deposited by the photon. Accordingly the energy deposited at that voxel increases by Δw. It is important to note that the weight of the photon is measured n terms of energy units.

3.1.3 Photon Scattering

The photon interaction at the interaction site results in the scattering of the photon. The angle of scattering is derived from the scattering function[22, 12] and the cosine of the scattering deflection angle (θ) is given as follows:

$$Cos(\theta) = \frac{1}{2g}\left(1 + g^2 - \left[\frac{1-g^2}{1-g+2g\varepsilon}\right]^2\right) \ if \ g \neq 0 \quad (21)$$

$$Cos(\theta) = 2\varepsilon - 1 \ if \ g = 0 \quad (22)$$

Where ε lies between 0 and 1 and g can have values from -1 to 1. Scattering is also determined by the azimuthal angle ψ which has a normal distribution from 0 to 2π determined using the relation:

$$\psi = 2\pi\varepsilon \quad (23)$$

The deflection and azimuthal angles are then used to determine the new direction of the photon after the scattering event. The unit vector directions in the x, y and z axis are as follows:

$$\mu_x' = \frac{Sin\theta(\mu_x\mu_z Cos\psi - \mu_y Sin\psi)}{\sqrt{1-\mu_z^2} + \mu_x Cos\theta} \quad (24)$$

$$\mu_y' = \frac{Sin\theta(\mu_y\mu_z Cos\psi - \mu_x Sin\psi)}{\sqrt{1-\mu_z^2} + \mu_y Cos\theta} \quad (25)$$

$$\mu_z' = \frac{-Sin\theta Cos\psi}{\sqrt{1-\mu_z^2} + \mu_z Cos\theta} \quad (26)$$

3.1.4 Creating Objects using Voxels

The MCX software allows users to define voxel space by assigning different optical properties to voxels. The software originally was used with a few media types. In this project different objects were created by using simple geometric equations which would assign voxels lying within a geometric shape. Thus a sphere, ellipsoid, cuboids were created using Matlab script. A binary file containing 'unichar' characters was created to designate voxels with different optical properties. The process of assigning regions is shown as in Figure 3.2[14].

0	0	0	0	0	0	0	0	0	0
0	0	0	0	0	0	0	0	0	0
0	0	0	1	1	1	1	0	0	0
0	0	1	1	1	1	1	1	0	0
0	0	1	1	1	1	1	1	0	0
0	0	1	1	1	1	1	1	0	0
0	0	1	1	1	1	1	1	0	0
0	0	0	1	1	1	1	0	0	0
0	0	0	0	0	0	0	0	0	0
0	0	0	0	0	0	0	0	0	0

Figure 3.2 Assigning voxels to regions[14]

3.1.5 Reflection at Object Boundaries

Since the object boundaries are defined by voxels, the voxel faces also form the interface between two media. Hence, the angle of incidence and reflection can be determined by determining the angle made by the photon with respect to the voxel boundaries of two voxels with different optical properties. The mechanism of determining the reflection interface is shown by the example in Figure 3[16]. The photon is assumed to be travelling from a medium to air denoted by the respective voxel properties. Each neighboring interface is calculated by calculating the time of flight from the current point in the photon trajectory. In the first example (a) in the figure, the interface C_1 is calculated from the position P_N and the properties of the neighboring voxel is determined. Since it is found to be of the same type, the shortest time of flight is calculated backwards from the next point P_{N+1} in the photon trajectory. Thus the interface C_2 is identified. Here both the voxels are seen to have different optical properties and hence, C_2 is determined

to be the reflection interface between the medium and air. The second example (b) in Figure 3.3 shows the photon trajectory through three such interfaces. In this case both C_1 and C_2 form the interfaces of voxels with the same optical properties and thus based on their orientation, the orientation of the interface C_3 is determined in a unique manner as each interface in the x, y and z direction can be passed only once when the step size is equal to one voxel edge length. Thus the process of calculating the time of flight backwards gives a unique way of determining the reflection interfaces. The reflection coefficient, calculated from the Fresnel's equation is then multiplied to the photon packet weight[16].
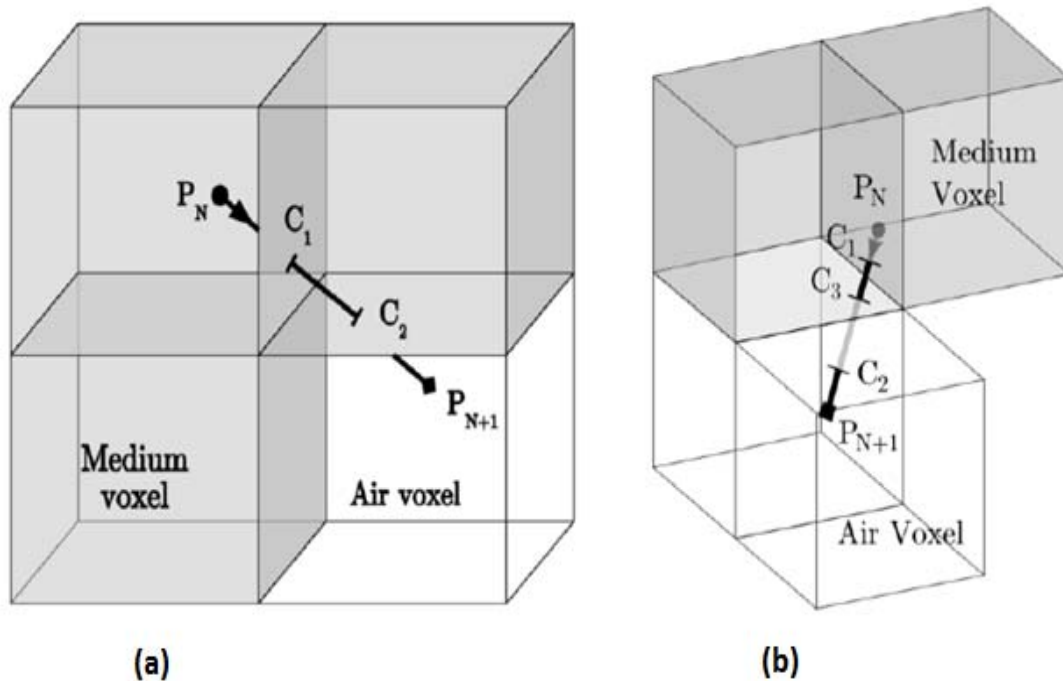
Figure 3.3 Mechanism for reflection between two mediums[16] (a) Photon path with two interfaces (b) Photon path with three interfaces

3.1.6 Time Gates and Photon Migration

The flight of the photon is binned in the form of user specified independent time-gates and is useful in addressing time related problems in photon migration. The fluence

is saved in the graphics memory known as global memory of the graphics card. Time gates are also divided into different groups and each group (containing multiple time gates) is run independently.

The use of graphics card limits the time taken to write into the global memory which is slow as compared to writing/reading from the constant and shared memories, which are smaller and insufficient in size as compared to the global memory. The reduction of global memory access is an area of research for designing efficient Monte Carlo software.

3.2 Simulation with Pencil Beam

The original code developed by Fang et al[16] simulated a light source to generate a pencil beam which was one voxel wide at the source (point source). The observations below show some of the simulations performed using this beam. Even though this beam does not resemble a 'real life' light source, it nevertheless is the foundation on which this research has been based, wherein the light source used in the actual scanner was simulated by using multiple point sources.

Some simple simulations were first performed in order to study the working of the original algorithm using the point source. Figures 3.4 and 3.5 show the fluence images from simulations performed by emulating a spherical object in the path of a pencil beam. The voxels designating the medium (water) have the following properties: absorption coefficient = 0.000001 mm^{-1}, scattering coefficient = 0.002 mm^{-1}, anisotropy factor = 1, refractive index = 1.3; while the object have been given the properties as: absorption coefficient = 3 mm^{-1}, scattering coefficient = 0.005 mm^{-1}, anisotropy factor = 0.935, refractive index = 1.3. In Figure 3.5, an object with a scattering coefficient = 0 is simulated while the absorption coefficient is the same as the previous. Thus Figure 3.5 represents an object with high absorption with no scattering.

The PCT scanner uses a laser beam which resembles a super-Gaussian distribution and hence, the Monte Carlo code needs to be modified so as to generate a real life laser beam profile.
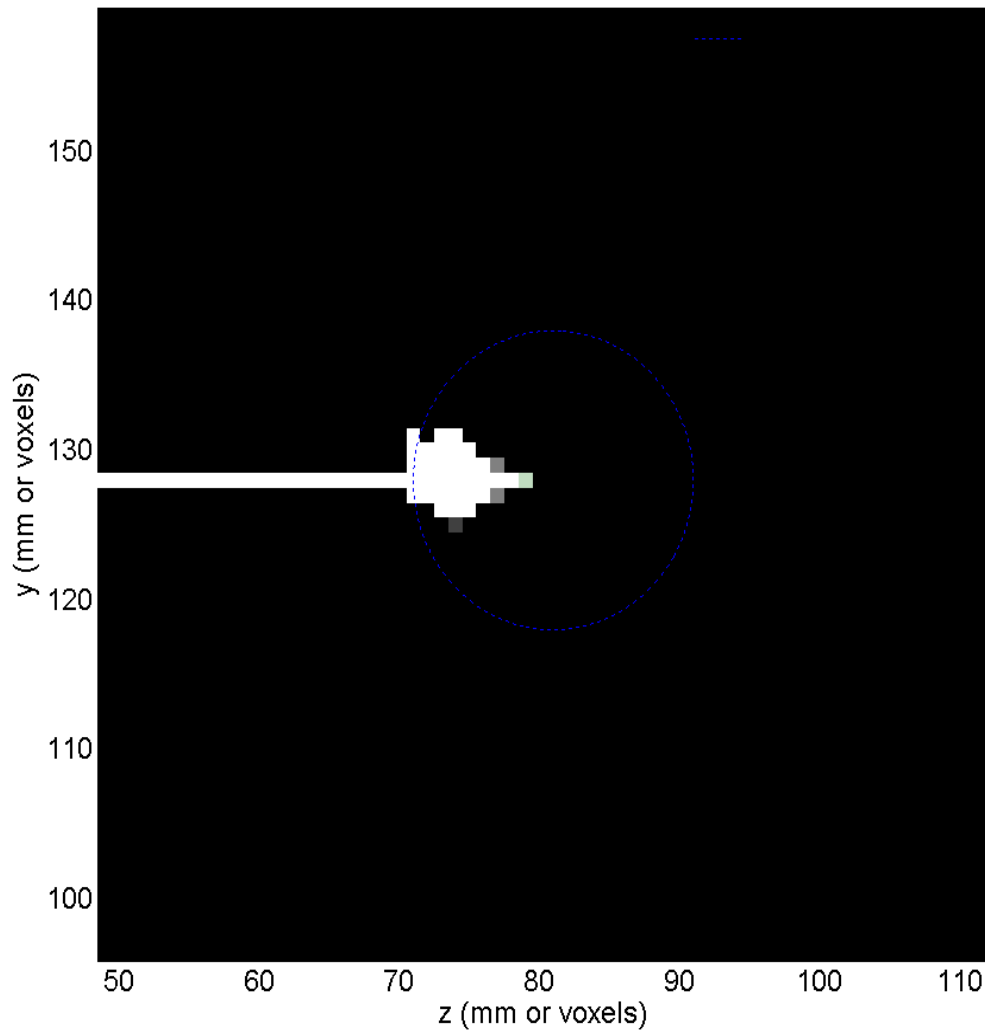
Figure 3.4 Fluence image of a Monte Carlo simulation. The radius of the sphere is 10 voxels, with each voxel having side equal to 1 mm. The medium surrounding the sphere has low scattering and absorption coefficients while the voxels within the sphere have been assigned absorption coefficient of 3 mm^{-1} and scattering coefficient of 0.005 mm^{-1}.
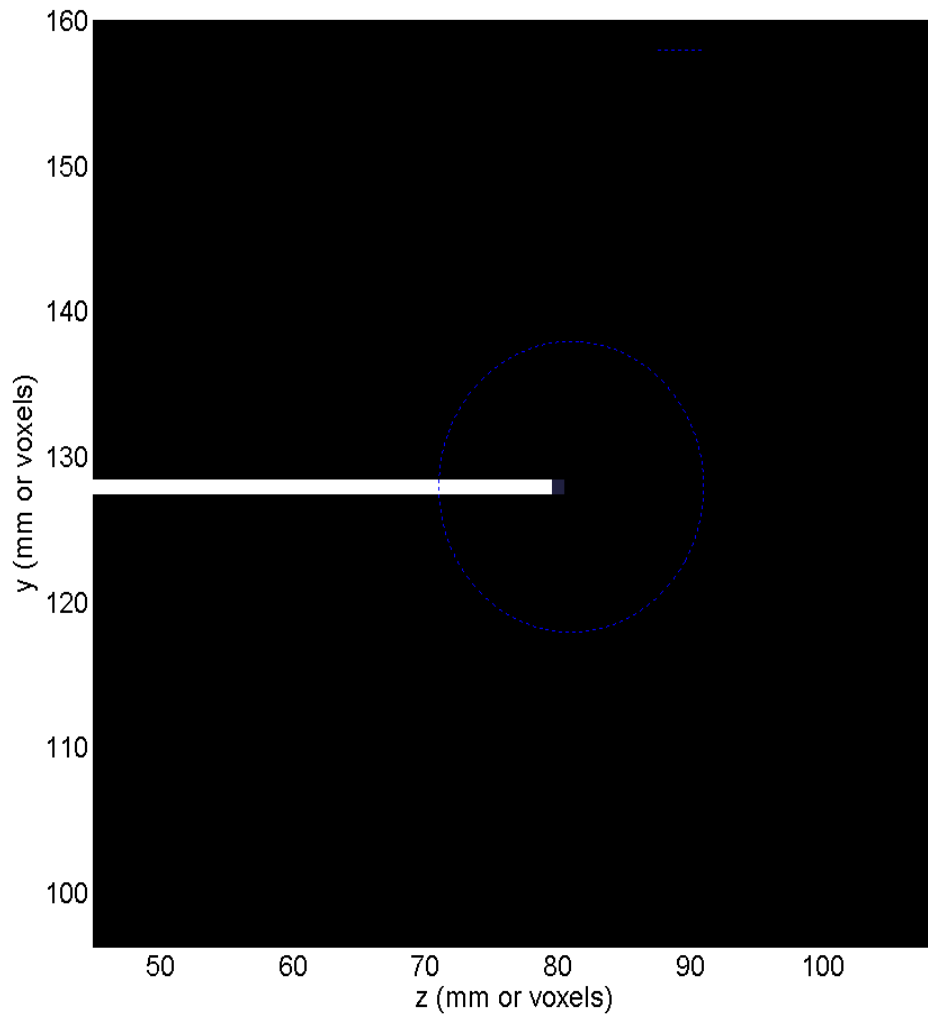
Figure 3.5 Fluence image of a Monte Carlo simulation. The radius of the sphere is 10 voxels, with each voxel having side equal to 1 mm. The medium surrounding the sphere has low scattering and absorption coefficients while the voxels within the sphere have been assigned absorption coefficient of 3 mm^{-1} and scattering coefficient of 0 mm^{-1}.

3.3 Generation of a Super Gaussian Beam

The laser beams used in various scanners have different beam profiles depending on the type of laser and optical path of the beam. Hence, a Monte Carlo simulation needs

to generate a beam which closely resembles, if not matches, the energy distribution of the real beam. Hence, in this study the existing Monte Carlo code was used and modified to generate a beam model which would resemble the super Gaussian beam distribution used in the Photoacoustic scanner.

In order to generate such a beam, an iterative approach was used to generate multiple pencil shaped beams which would be used to create a resultant beam which would have the divergence of a real laser beam. A probability distribution function whose output distribution resembled the super Gaussian shape was used. The magnitude distribution function of the beam is given as follows:

$$A = A_0 e^{-\left(\frac{1}{2}\right)\left(\frac{r}{10}\right)^5} \quad (27)$$

The direction of the beam is given in the form of the directional vectors which are generated using random angle sampling. The angle between two vectors is constant and the incremental angle is given as:

$$\theta_{inc} = tan^{-1}(1/z) \quad (28)$$

Here, z is the distance between the source and the object along the azimuthal axis. Thus the magnitude is uniformly distributed along by using equal number of incremental beam angles along the x and y axis. Figure 3.6 shows the quiver plot of the directional vectors while Figure 3.7 shows the magnitude plot of the beam.

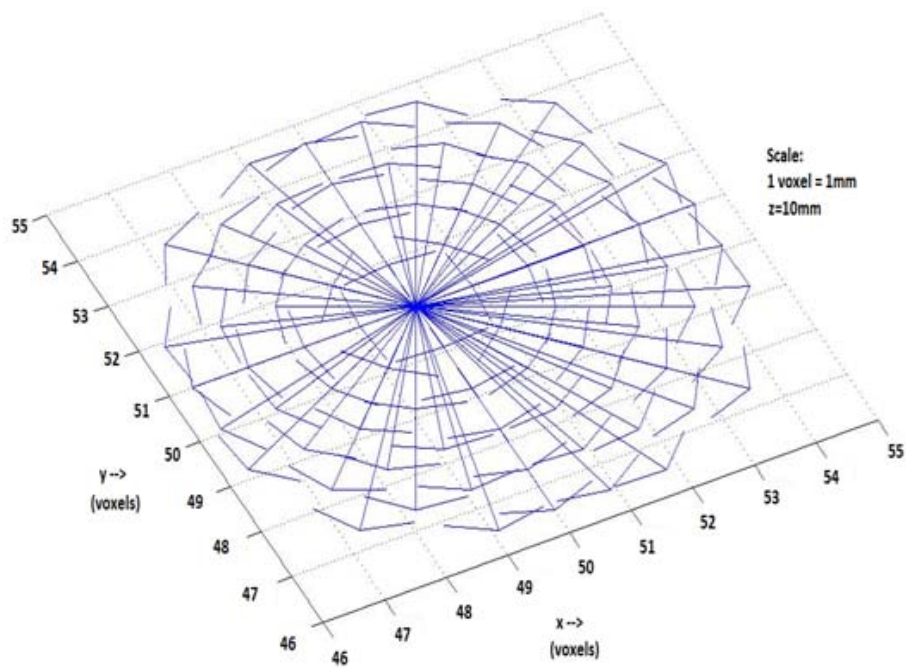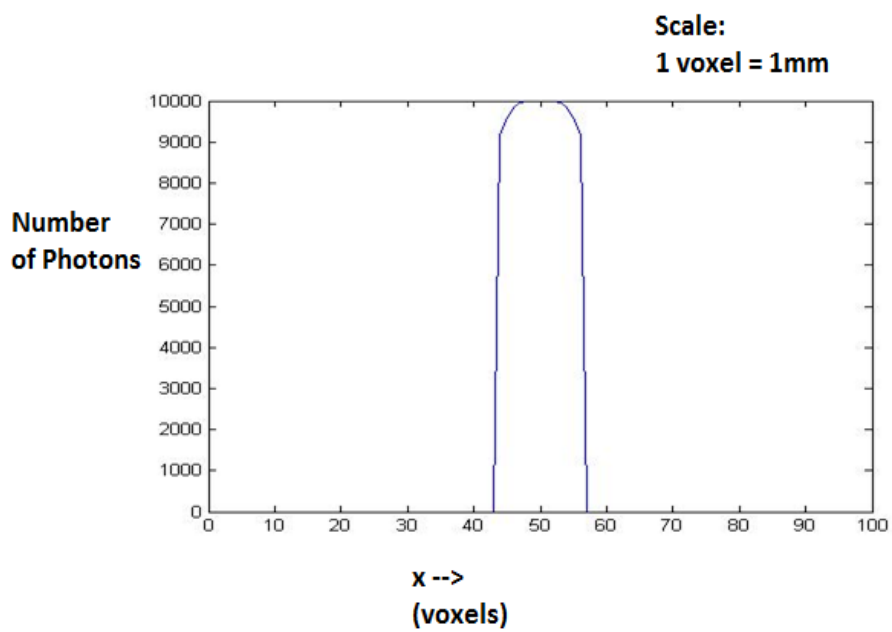Figure 3.6 Quiver plot of 3 dimensional vectors of the super Gaussian beam profile

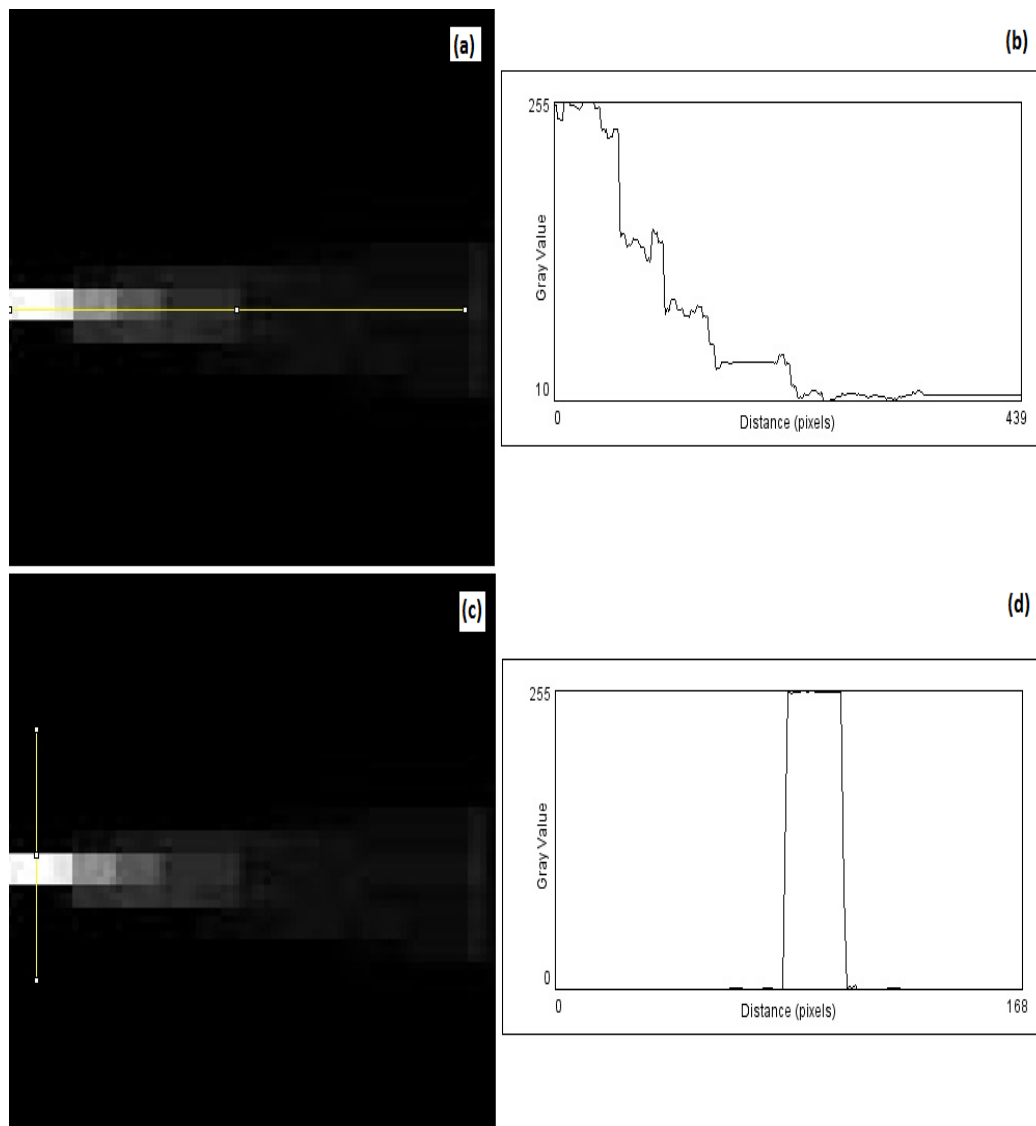Figure 3.7 Magnitude plot of the beam profile

Figure 3.8 Simulation results of beam profile: (a) & (c) show the gray scale images of normalized beam fluence profile as generated by the Monte Carlo code. (b) & (d) show the corresponding cross sectional fluence graphs which have been normalized to their gray scale values.

4. RECOVERY OF ABSORPTION COEFFICIENTS USING ITERATIVE ALGORITHM

4.1 Iterative Recovery Method

The focus of this study is to quantify the process of near infra-red (NIR) absorption and thermoelastic conversion of molecules, which show high photoacoustic properties. This conversion process depends on the optical absorption coefficient of the molecules and hence, one must first derive this in order to be able to extract the thermoelastic conversion coefficient. Thus the success of this technique depends on the accurate prediction of the absorption coefficient of the tissues being imaged.

To accomplish this goal, the photon fluence distribution within the tissue is required. Hence to determine this in, an iterative algorithm has been developed to determine the photon fluence without a priori knowledge of the absorption coefficient. It utilizes the direct relationship between the fluence and the energy distribution as suggested in Equation 16. Thus the fluence output in every iteration of the Monte Carlo is used along with the energy distribution from the PCT scanner in order to predict the absorption coefficient of each voxel is predicted on a voxel by voxel basis. Thus the original Monte Carlo code is used in the form of a simulated routine to accurately predict the absorption coefficient of the imaged molecules. The voxel by voxel comparison followed in this iteration is the unique feature of this study.

The flowchart for the recovery of the absorption coefficient is given in Figure 4.1[14]. In order to determine these quantities for every voxel, the Monte Carlo must be able to generate a voxelated map of the fluence and the energy distribution. The energy-fluence relationship is used as stated in Equation 16.

In every such iteration the value of recovered μa is updated as follows:

$$\mu_a^{k+1} = \hat{H}/\phi^k \quad (30)$$

Here $\hat{H}$ is a reference energy map, μ_a^{k+1} is the recovered absorption coefficient and ϕ^k is the fluence profile obtained for the iteration k. A merit function is used to compare the two energy maps. In case of a mismatch, the value of μ_a^{k+1} becomes the input value for the next simulation run. The design of the merit function plays a critical role in ensuring the accuracy of the iteration routine.
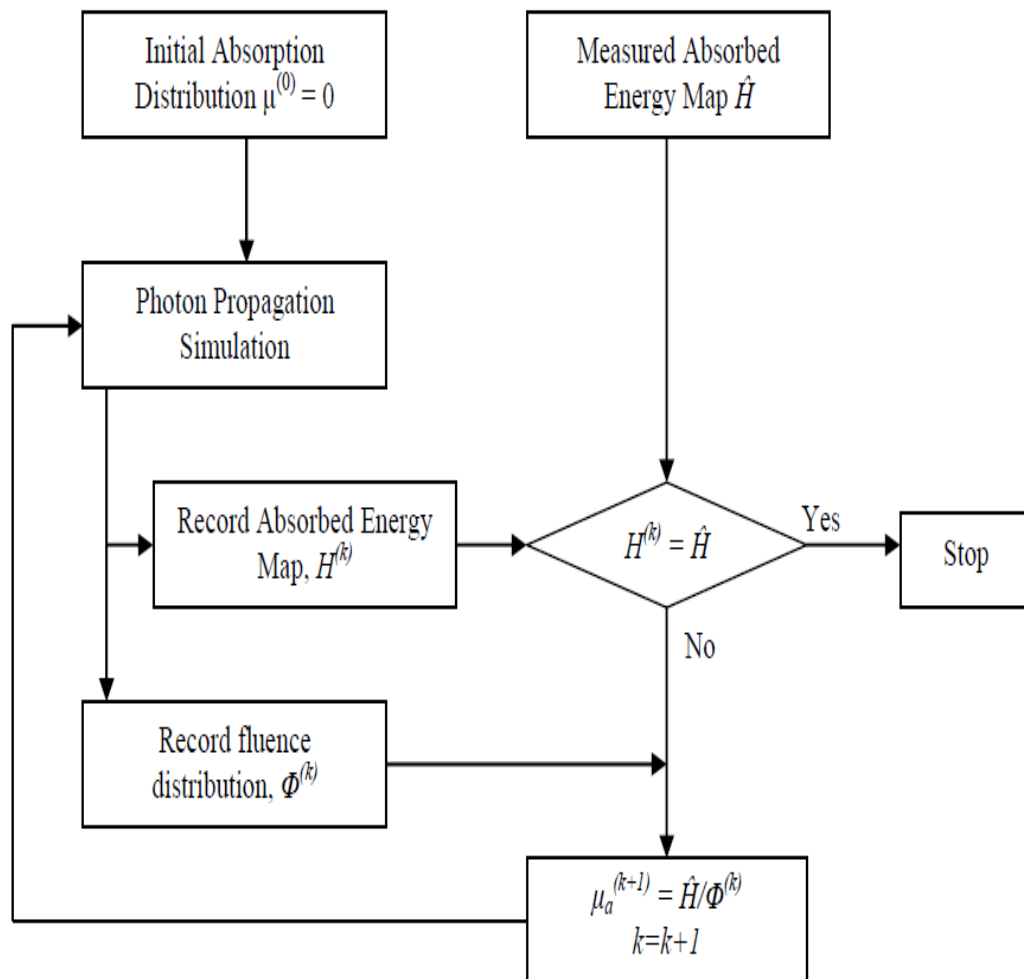

Figure 4.1 Iterative algorithm flowchart for recovery of absorption coefficient[14]

4.2 <u>Merit Function</u>

The merit function is the criteria used to determine the accuracy of match between the Monte Carlo energy map and the reference energy map. The magnitude of statistical errors arising from this mismatch is the best possible prediction of the accuracy of the absorption coefficient recovery. The two maps are compared on a voxel by voxel basis and the resultant percentage mismatch is analyzed. Two kinds of errors are considered: (1) percent difference between the two individual voxels, and (2) percentage of total number of matching voxels. In this study a match of 95% is considered as a match for both the above criteria. The statistical errors are analyzed and it is observed that they reduce after every iteration thereby demonstrating the accuracy of the merit function. The results are depicted in the next section.

Thus the following factors affect the accuracy of this iterative technique: (1) the merit function, (2) number of photons simulated, and (3) range of absorption coefficients within the tissues. In this study, the reference map has been generated by using a Monte Carlo simulation with known optical properties of tissues[1, 3, 11, 12, 14, 17].

4.3 <u>Simulation and Iterative Recovery Results</u>

4.3.1 <u>Optical Properties of Tissues</u>

Table 4.1 shows the list of optical properties such as the absorption coefficient (μa), reduced scattering coefficient ($\mu s1$), anisotropy factor (g) and refractive indexes (n) used in the simulations:. The scattering coefficient, anisotropy factor and refractive index were mostly unchanged. The purpose of this simulation study was to recover the absorption coefficient for constant values of the other three optical parameters. A total of about 20 simulations were performed using different combinations of the above properties. However due to time and space constraints the details of only one such simulation has been shown in Section 4.2.3. A summary of these simulations is shown in the Figure 4.2.

Table 4.1 Optical properties of tumors.

μ_a (mm^{-1})	μ_s^{-1} (mm^{-1})	g	n
0.001	0.9	0.91	1.3
0.004	0.9	0.91	1.3
0.005	0.9	0.91	1.3
0.0075	0.9	0.91	1.3
0.01	0.9	0.91	1.3
0.02	0.9	0.91	1.3
0.025	0.9	0.91	1.3
0.05	0.9	0.91	1.3

The different optical properties as shown in table 1 were simulated. The number of iterations required for the algorithm to converge increases with an increase in the optical absorption coefficient. The higher the absorption coefficient of the object, greater is the time required for the iterative routine to converge. It must be noted that the iteration begins with absorption coefficient of the object set to zero, while those of the medium are set to the known values. Hence, if the difference between the two is large, then we need more computation time to predict the absorption coefficient of the object. Figure 4.2 confirms this reasoning, wherein μa = 0.05 requires 7 iterations to converge as compared to 4 iterations for μa = 0.001. More work needs to be done, to study the dependence of convergence on the relationship between the optical properties of the tissue from the surrounding medium.

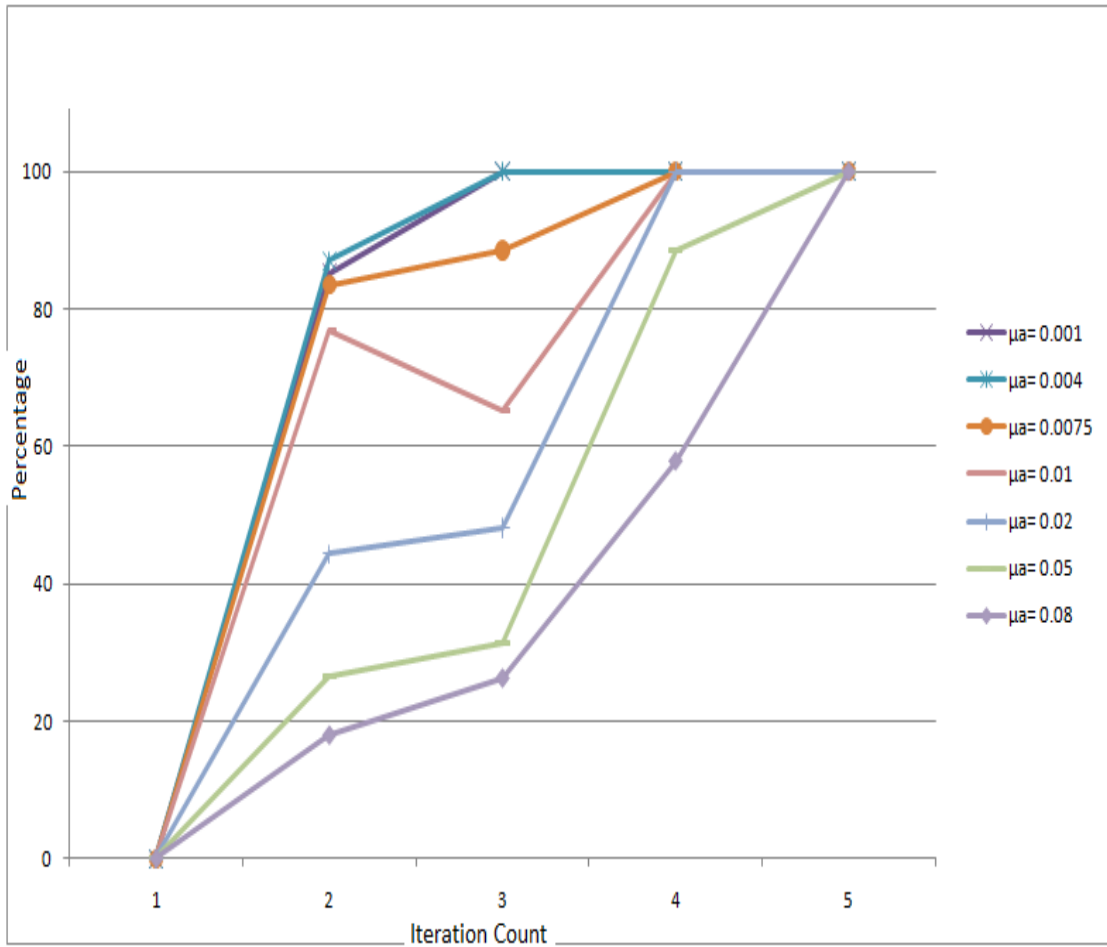Figure 4.2 Iteration count versus percentage for simulations with different optical absorption coefficients μ_a. More number of iterations (i.e., more computational time) is required with increase in absorption coefficient of the imaged tissues.

4.3.2 Tumor Model

Figure 4.3 shows a typical model of a tumor as depicted in a Monte Carlo simulation.
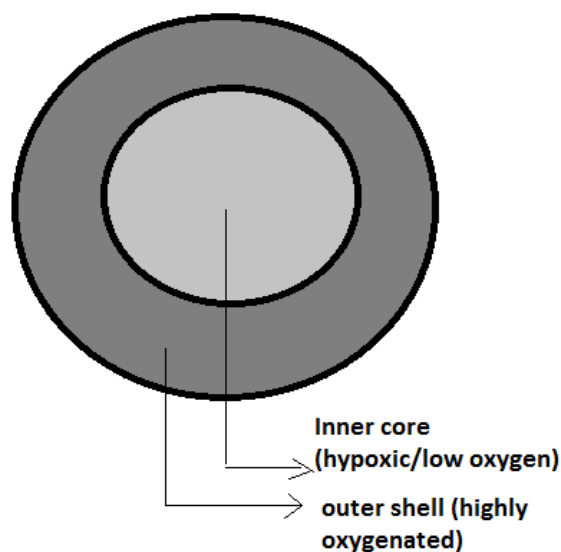
Figure 4.3 Structure of a tumor model. The inner core is hypoxic or devoid of oxygen content while the outer core has excess of blood vessels. This creates a difference in optical properties between the two regions.

As stated in the figure, the outer shell consists of a highly dense network of blood vessels and is hence, rich in oxygen content, while the inner core is devoid of oxygen. This creates a difference in the effective absorption coefficient values between the two regions. This study tries to depict this model in its simulation studies in order to emulate real time tumors.

4.3.3 Sample Simulation Results

The following figures show the results for one such simulation. The tumor model was simulated. The figures include normalized fluence images, fluence profile graphs and the graph of iteration count versus iterative percentages.

In this sample simulation, the following optical properties were assigned: The inner hypoxic core of the tumor was assigned absorption coefficient of 0.001 mm-1, reduced scattering coefficient = 0.9 mm-1, anisotropy factor g = 0.91 and refractive index = 1.3. The outer shell of the tumor had absorption coefficient = 0.025 mm-1, reduced scattering coefficient = 0.9 mm-1, anisotropy factor g = 0.91 and refractive index = 1.3. The medium had absorption coefficient = 0.002 mm-1, reduced scattering coefficient = 0.000001 mm-1, anisotropy factor g = 1 and refractive index = 1.3. These were the values assigned to obtain the reference energy map. During the iteration recovery cycle, the voxels lying in the region of interest were assigned the same optical properties as above, however the absorption coefficient of these voxels was set to 0. Thus after every iteration the absorption coefficient was updated until the two energy maps finally converged as determined by the merit function.

Figure 4.1 (a) shows the gray scale image of fluence (units = 1/m2s) which has been normalized. The two concentric circles show the inner and outer regions of the tumor. Figure 4.4 (b) shows the corresponding normalized fluence plot along the z axis. The tumor extends from z = 47 to z = 57. The figure shows the exponential decay of the light fluence along the z axis within the tumor.

Figure 4.5 shows the gray fluence images, similar to that shown in Figure 4.4(a) for various iterations. It is important to note that the fluence and energy maps converge with the reference maps at the 6th iteration. Hence, the images (f) and (g) in Figure 4.5 look alike. A more descriptive version of this iterative convergence is shown in Figures 4.6, 4.7 and 4.8, which show the fluence plots along the x, y and z axis respectively for iterations 1-6 and the reference. The fluence plots are seen to converge with the reference fluence at iteration 6. The absorption coefficient obtained after iteration 6 shows greater than 95% match as decided by the merit function. To further investigate the convergence of recovered absorption coefficient, the systemic errors along the x, y and z axis have been plotted in Figure 4.10 along with the corresponding gray scale maps. The systemic error is the ratio of the difference in the reference absorption coefficient and the measured

absorption coefficient to the reference absorption coefficient value, i.e., (μref - μmeasured)/ μref. Thus it is seen that the systemic error reduces with increase in iteration count and is least when the two energy maps converge at the 6th iteration. Another interesting phenomenon observed is the dependence of the systemic error on the distance from the light source along the azimuthal direction. This could be due to the decrease in the number of photons as we travel further away from the beam. On the other hand, the systemic error in the x-y plane is fairly constant. Figure 4.9 shows the absorption coefficient map in gray scale at iteration 6. The iteration count versus percentage is plotted in Figure 4.11. The convergence to 100% occurs at iteration 6.
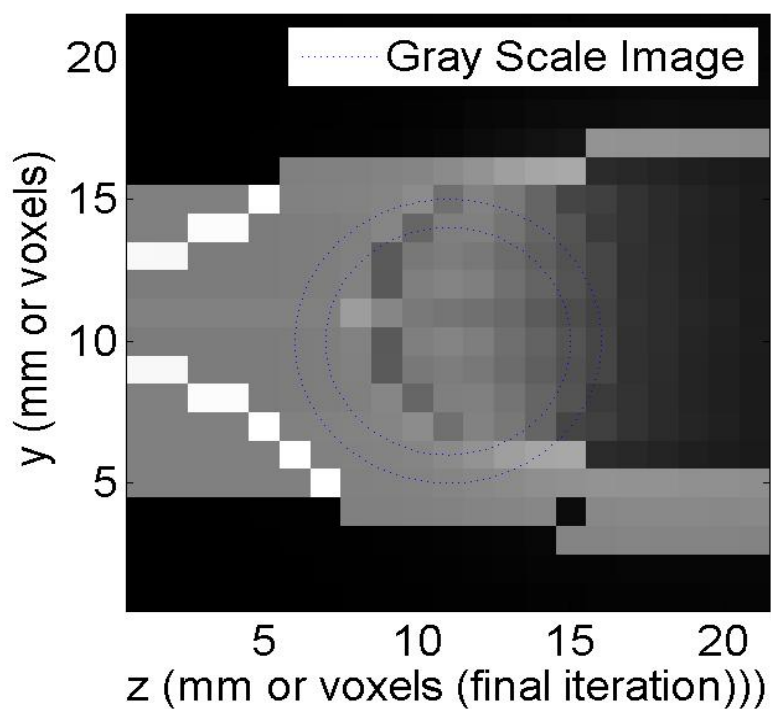
Figure 4.4 (a) Gray Scale image of fluence distribution
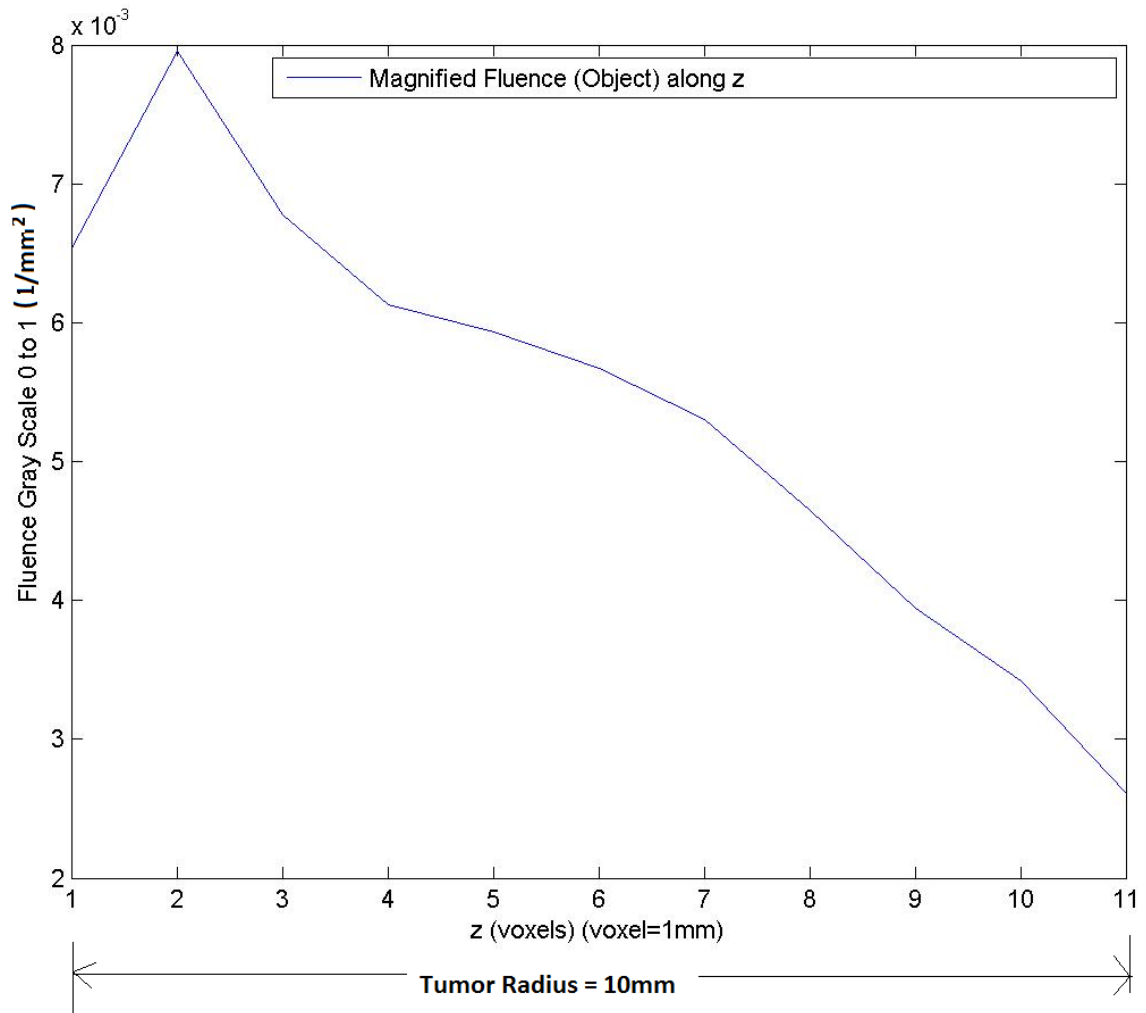
Figure 4.4 (b) Magnified fluence along center of the object
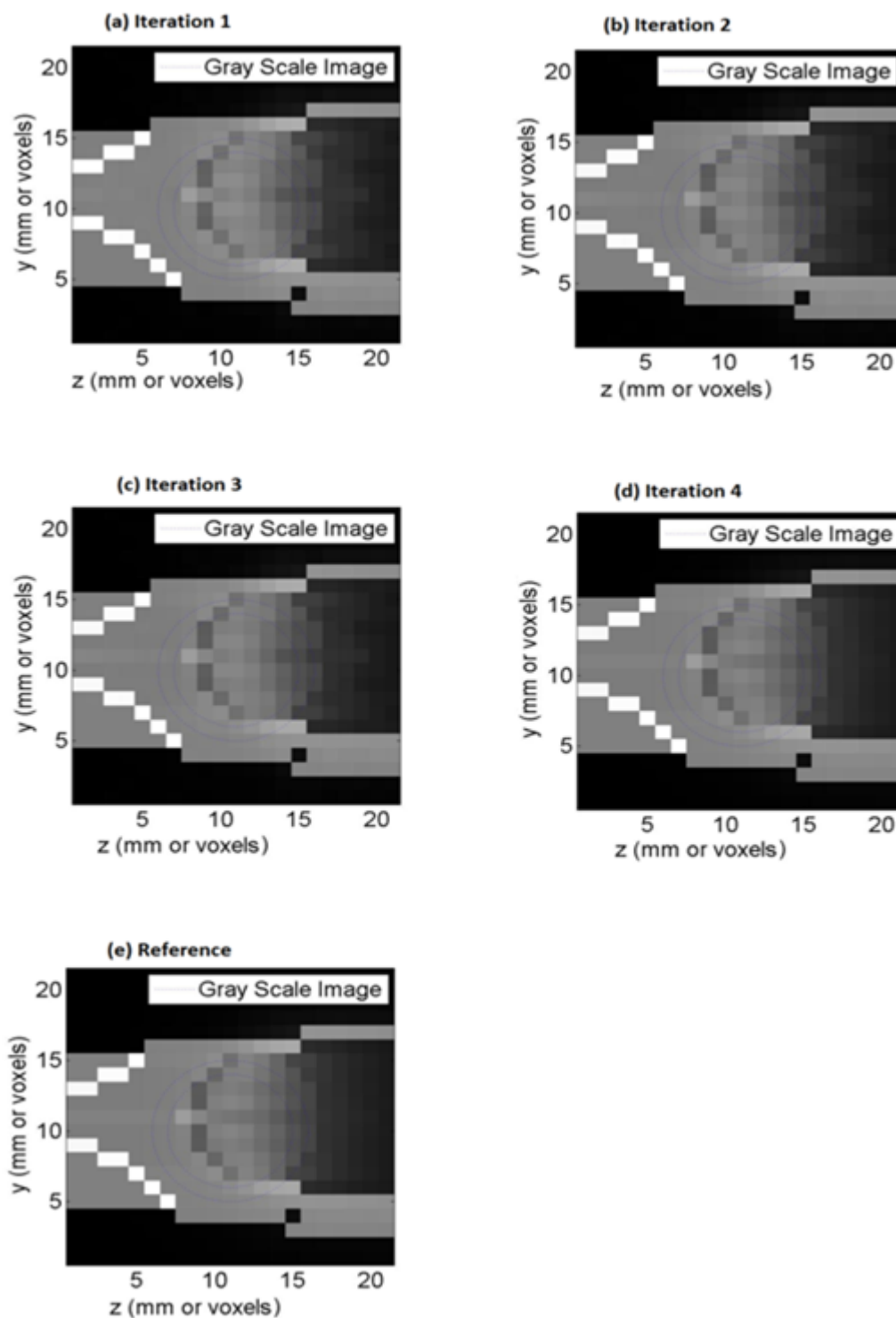
Figure 4.5 Gray scale fluence images in x-y plane at z = 50mmg. Figures (a) - (d) show fluence images for iterations 1 to 4 and (e) shows the reference fluence image
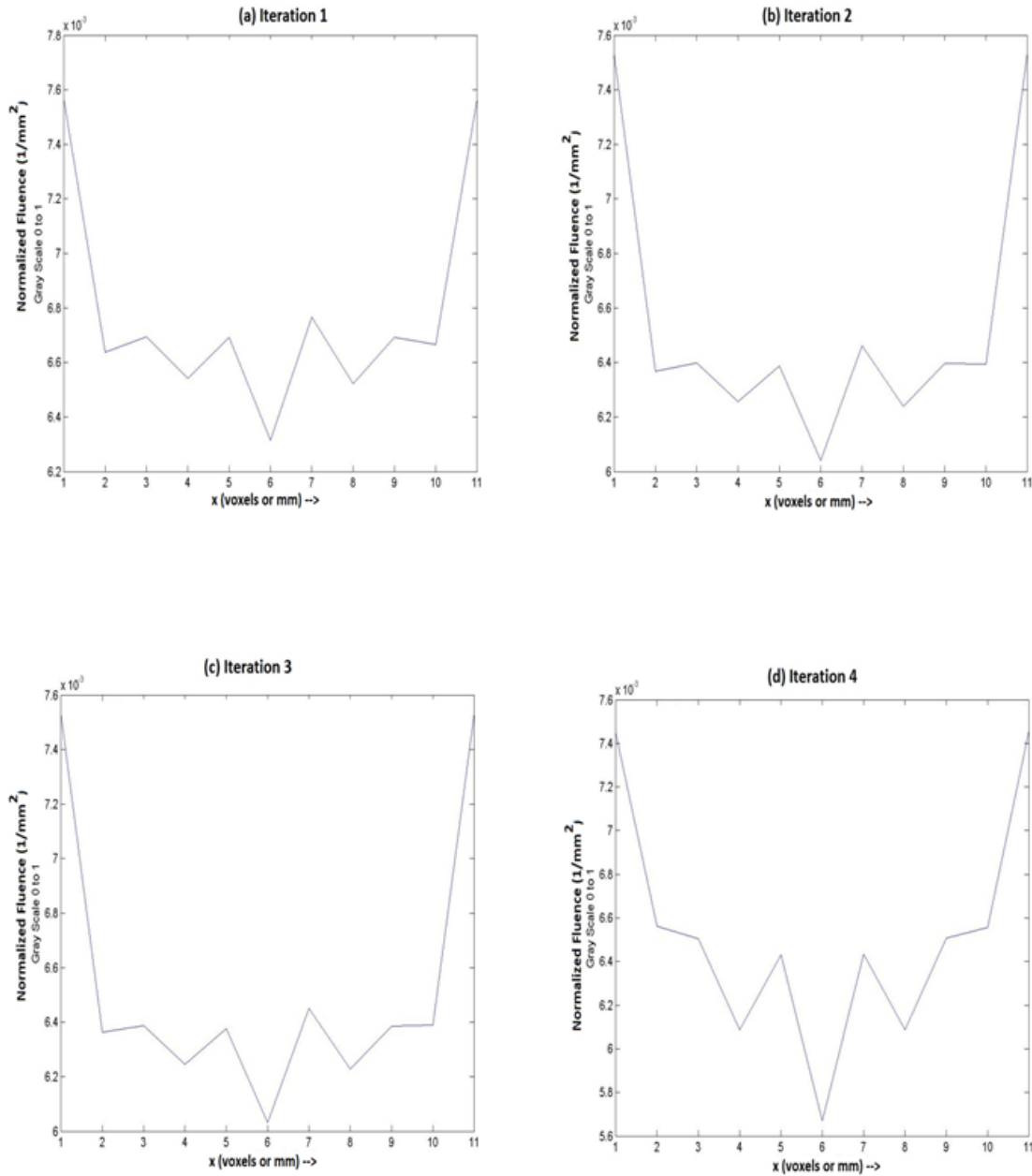
Figure 4.6 (a) – (e) Fluence plots across the object along x axis: Figures (a) to (d) show the normalized fluence graphs for iterations 1 to 4. Figure (e) shows the reference fluence.
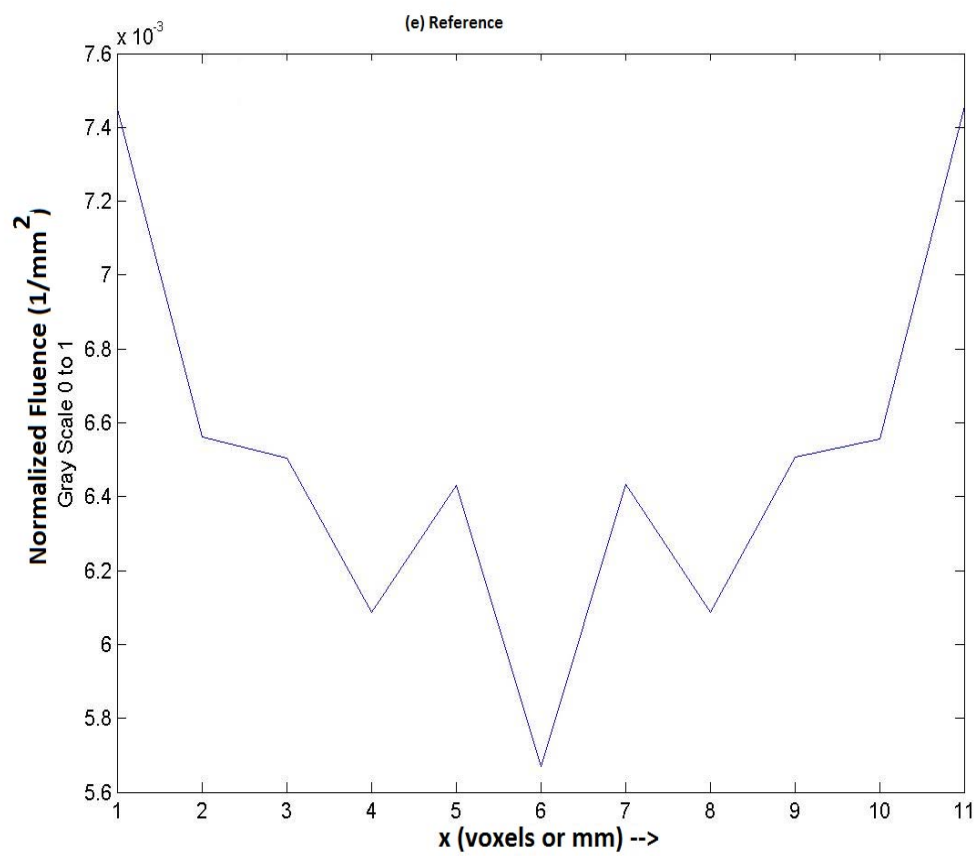
Figure 4.6 (a) – (e) Continued
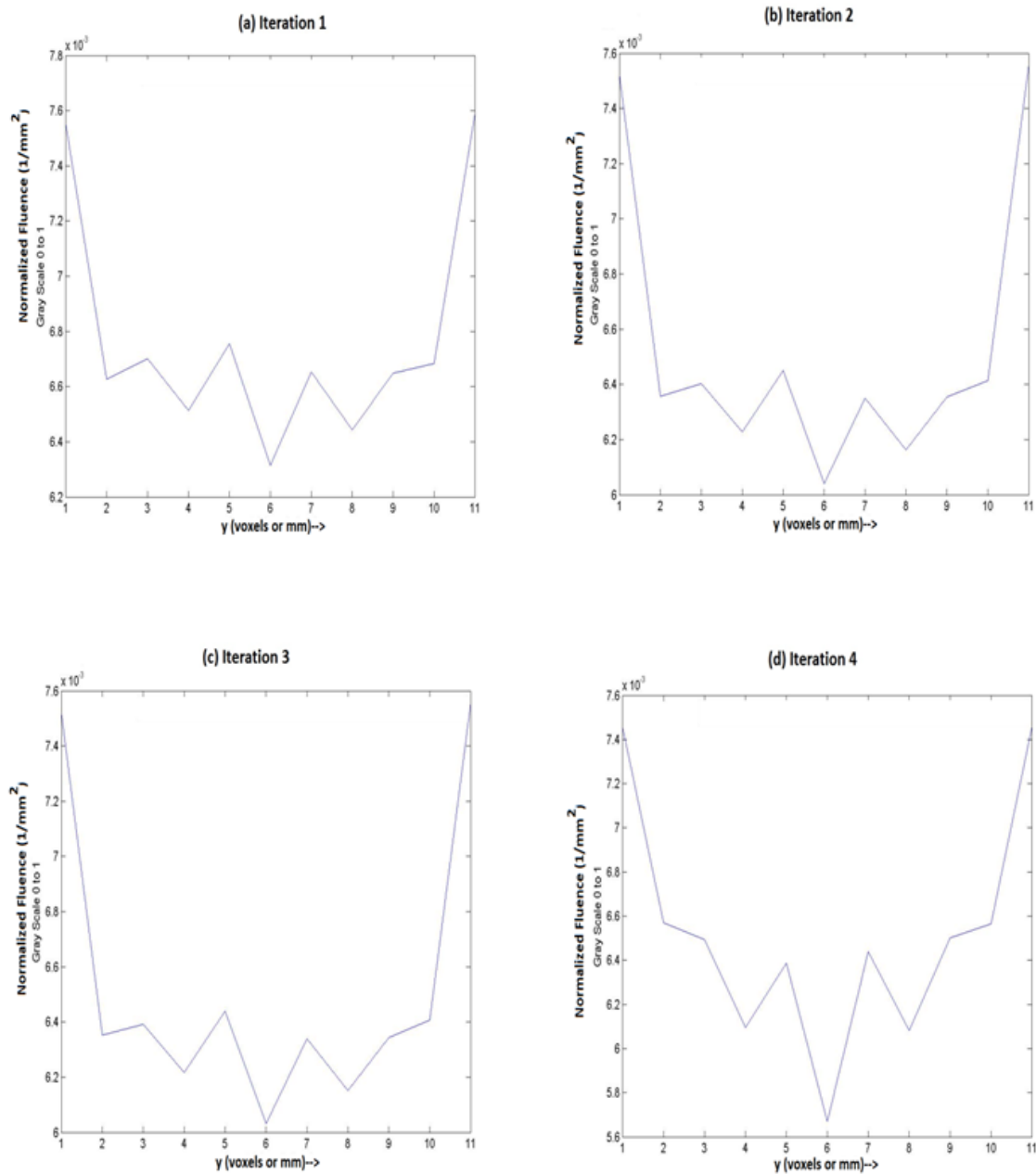
Figure 4.7 (a) – (e) Fluence plots across the object along y axis: Figures (a) to (d) show the normalized fluence graphs for iterations 1 to 4. Figure (e) shows the reference fluence graph.
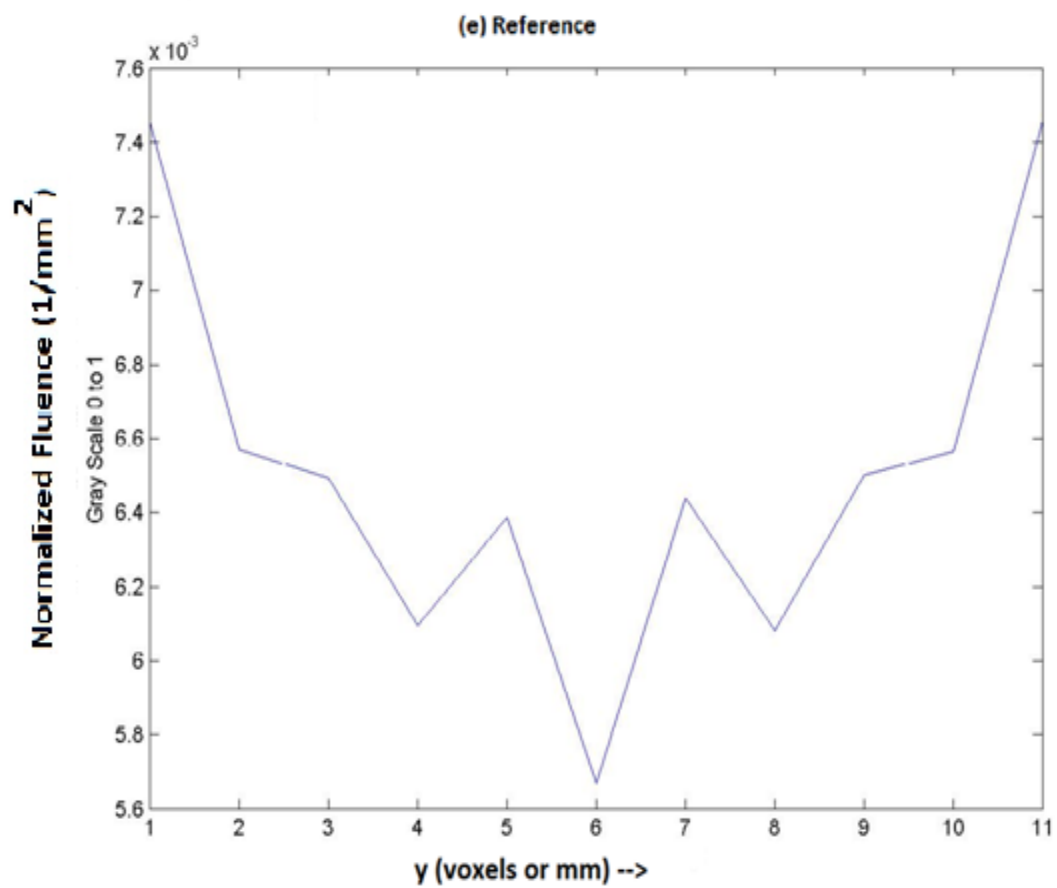
Figure 4.7 (a) – (e) Continued
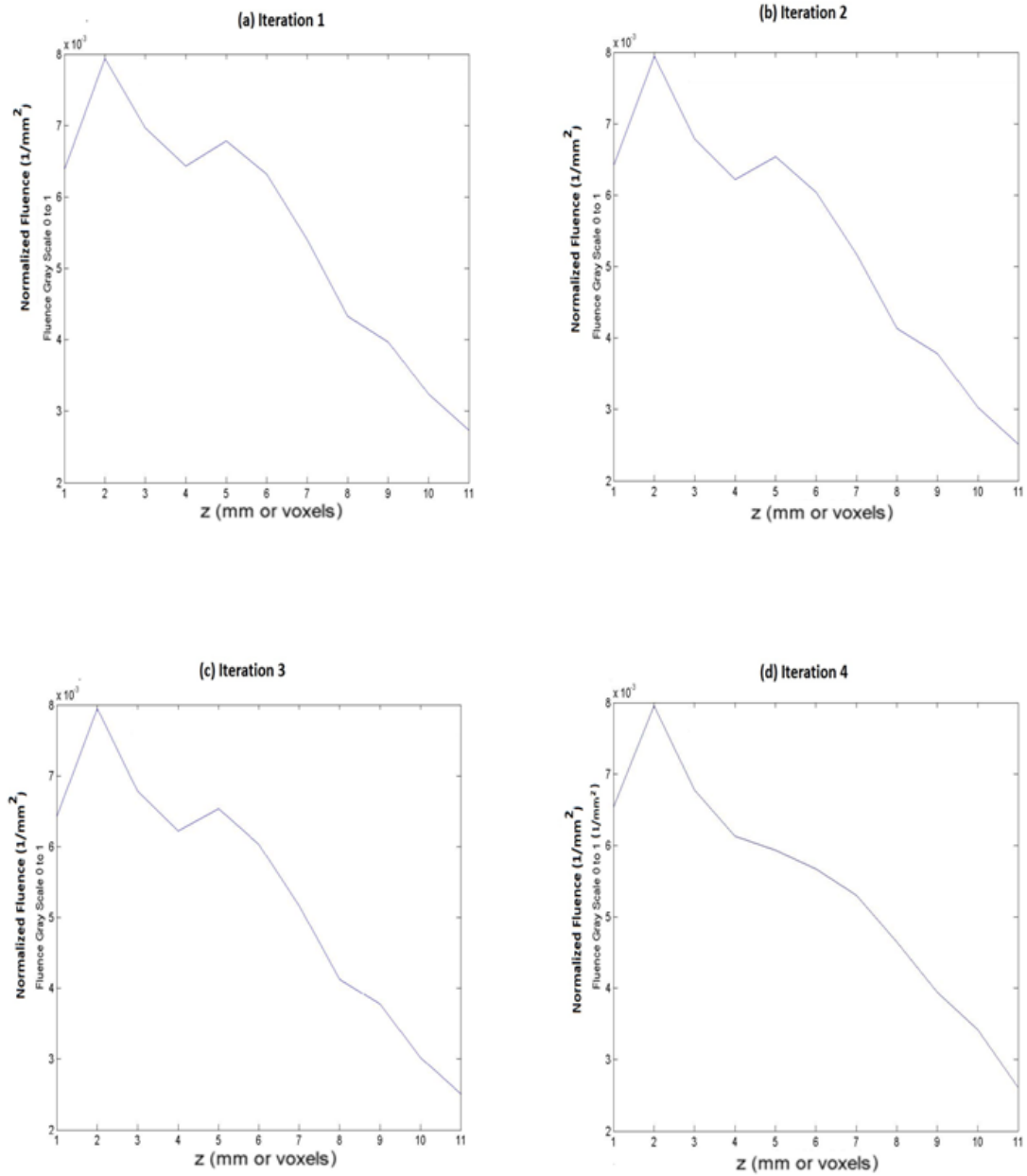
Figure 4.8 (a) – (e) Fluence plots across the object along z axis: Figures (a) to (d) show the normalized fluence graphs for iterations 1 to 4. Figure (e) shows the reference fluence graph.
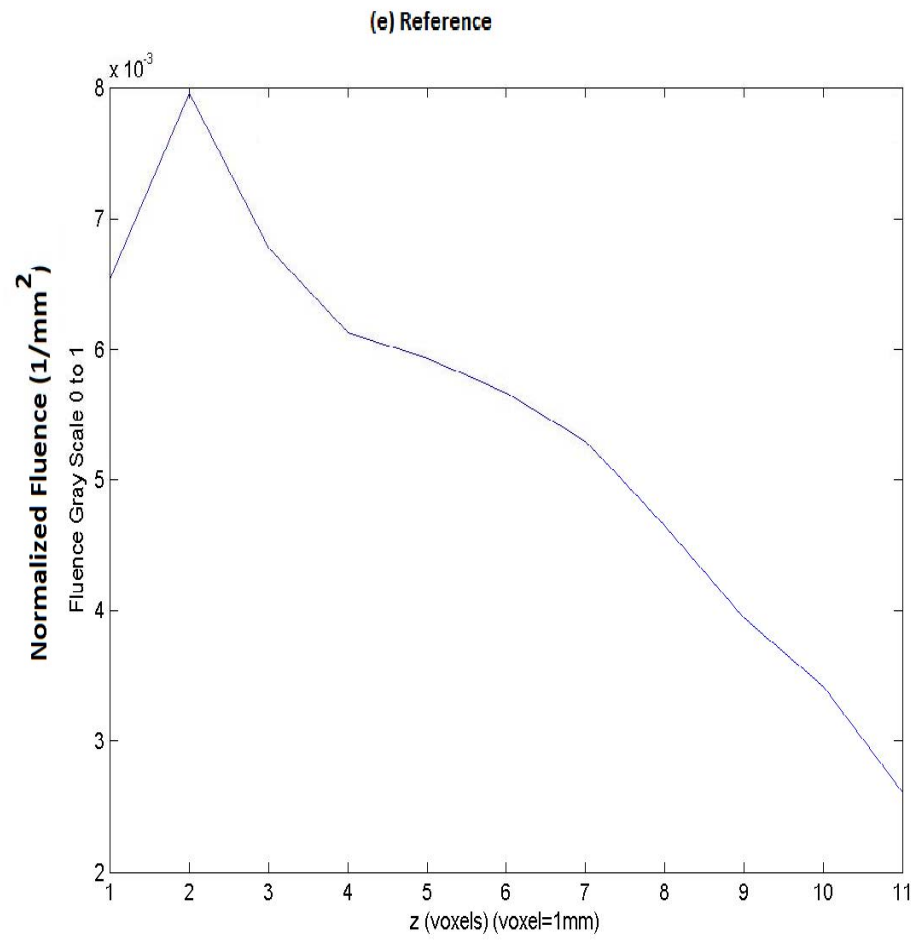
Figure 4.8 (a) – (e) Continued
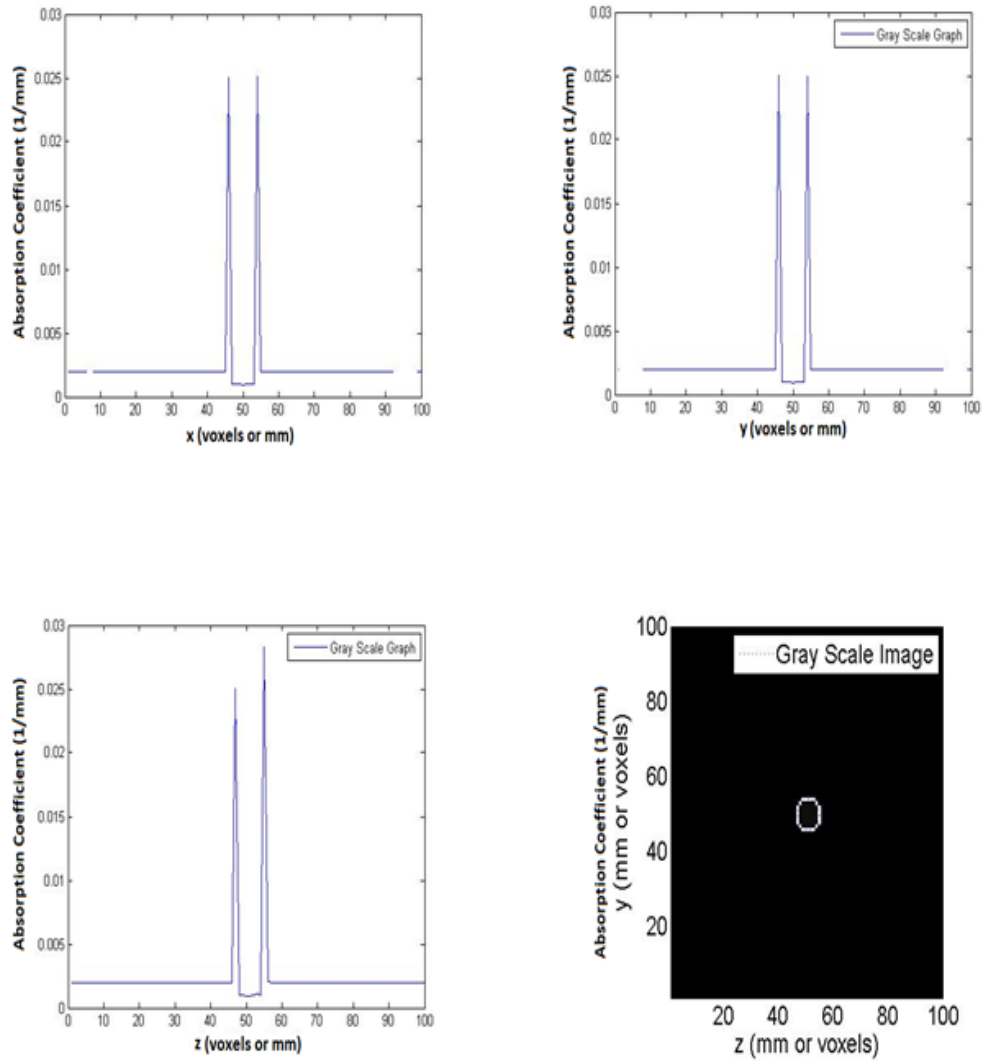
Figure 4.9 Recovered absorption coefficients along (a) x, (b) y and (c) z axis, and the corresponding gray scale image of absorption coefficient map. Note that the absorption coefficients are symmetrical in x, y and z directions throughout the spherical tumor.
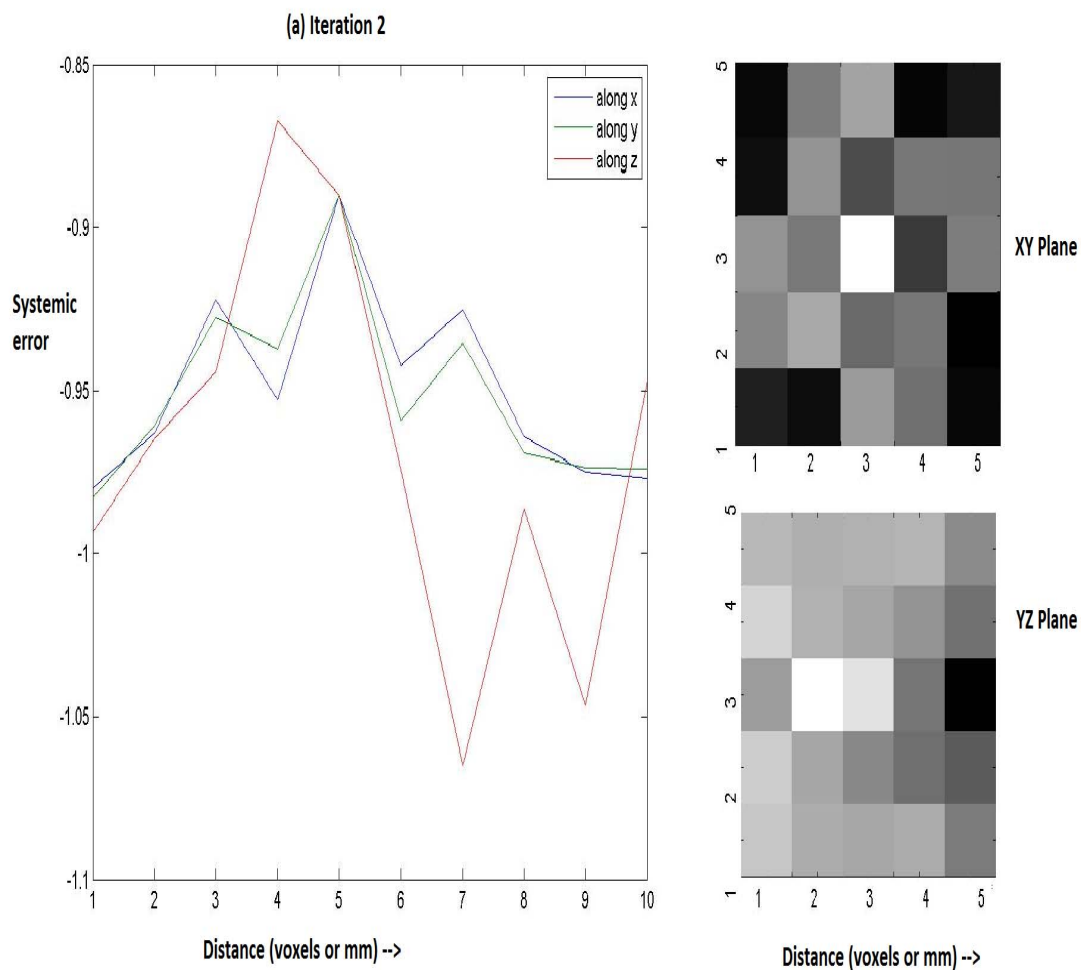
Figure 4.10 (a) – (c) Systemic error plots and maps. Figures (a) - (c) show the plots of systemic error for iterations 2 - 4 as a function of distance along x, y and z axis in the region of interest. Also shown are the corresponding gray scale systemic error maps in the x-y and y-z plane within the core of the tumor at z = 50mm. The merit function shows convergence over the entire tumor. Note that the systemic error for iteration 1 is 100% or 1 and is hence ignored.
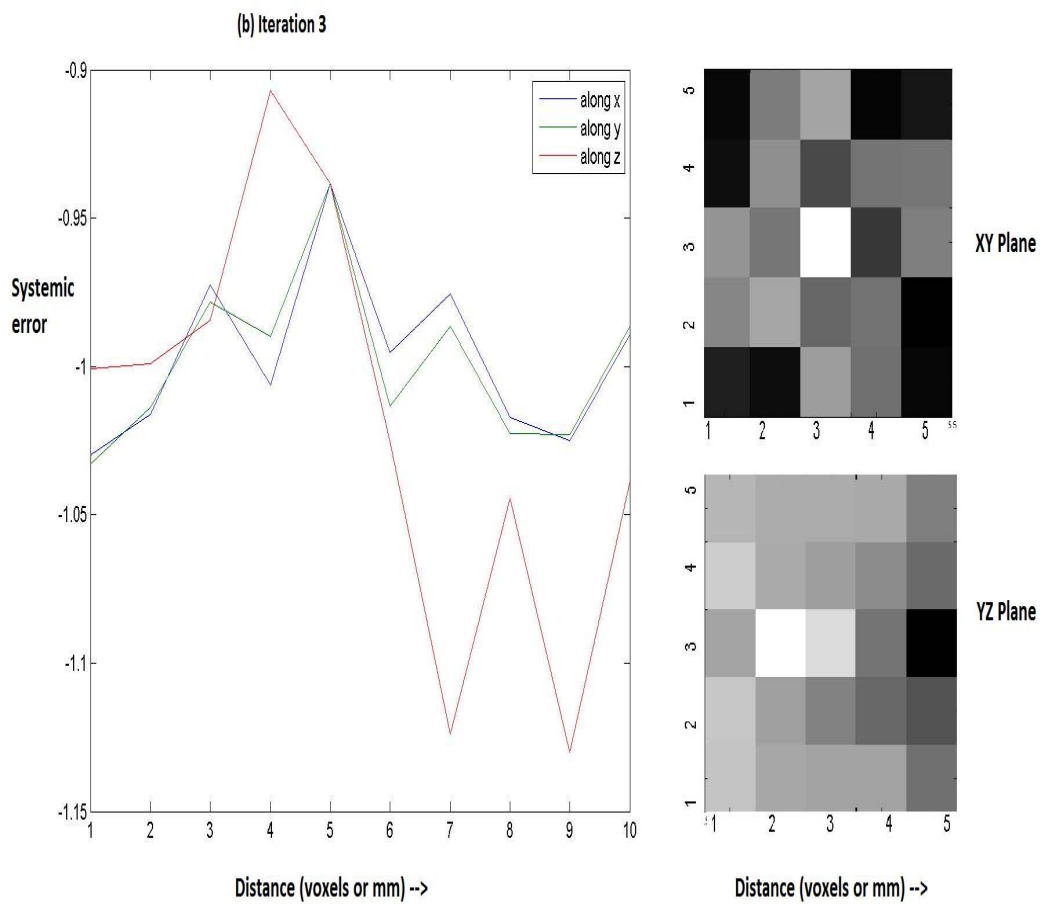
Figure 4.10 (a) – (c) Continued
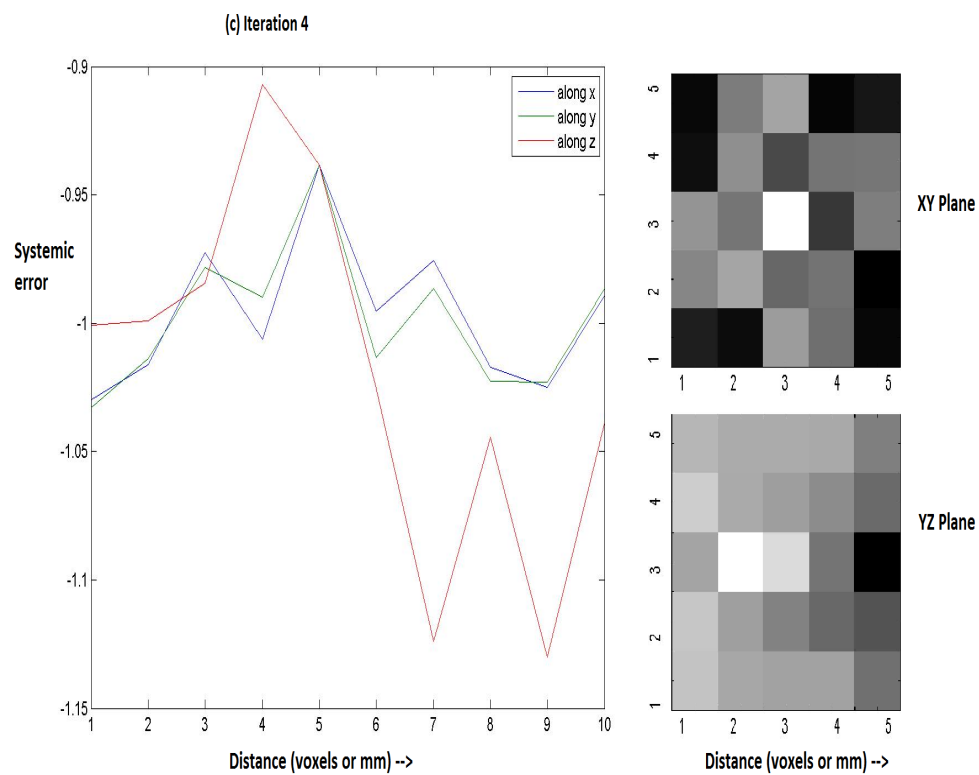
Figure 4.10 (a) – (c) Continued
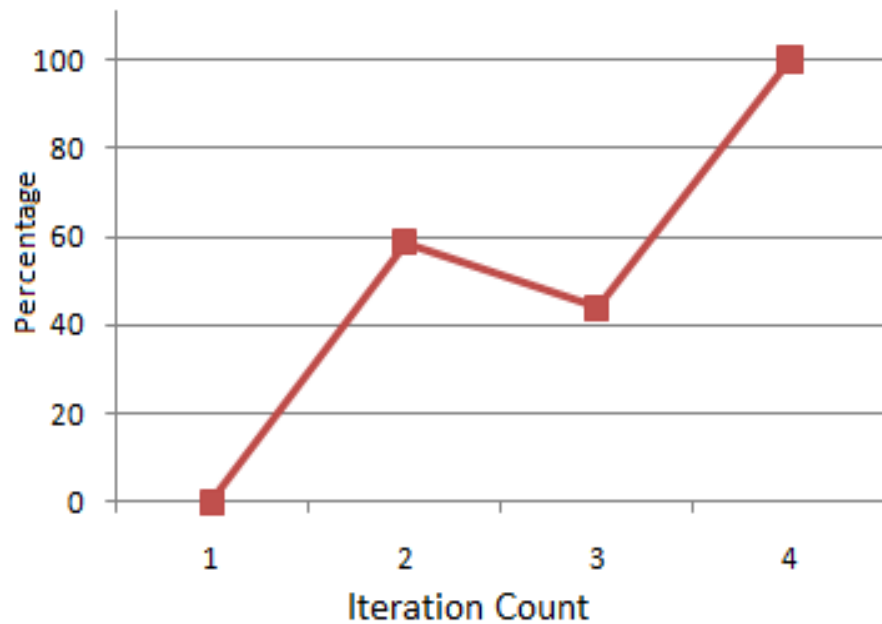
Figure 4.11 Plot of iteration count versus percentage

4.3.4 Change in Region of Interest

The region of interest defines the region in which the iterative algorithm operates. It is the area over which the absorption properties are adjusted after each iteration, so as to achieve a match between the reference and simulation energy maps. The merit function is used to determine the criteria for convergence. As discussed earlier a convergence of 95% or greater is considered as the criteria to achieve a successful recovery of absorption properties.
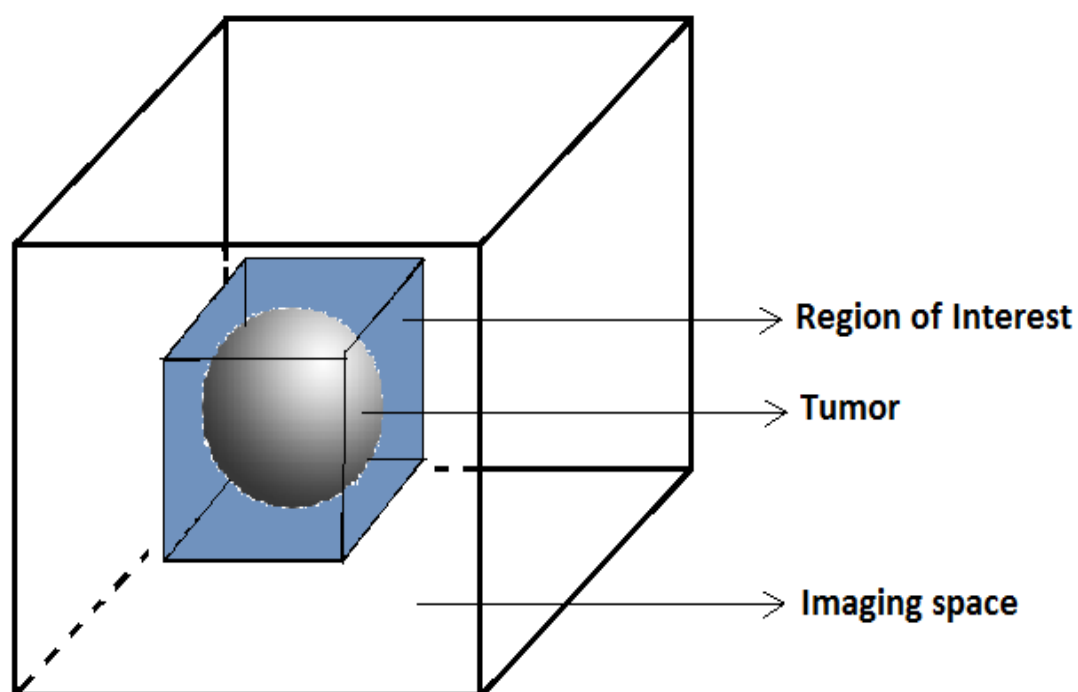
Figure 4.12 Region of interest. The large cube shows the imaging domain while the sphere shows the tumor as depicted within this imaging space. The blue cube surrounding the sphere is the region of interest. The region of interest can be varied in both size and position depending on the area of interest for iterative recovery of the absorption coefficient.
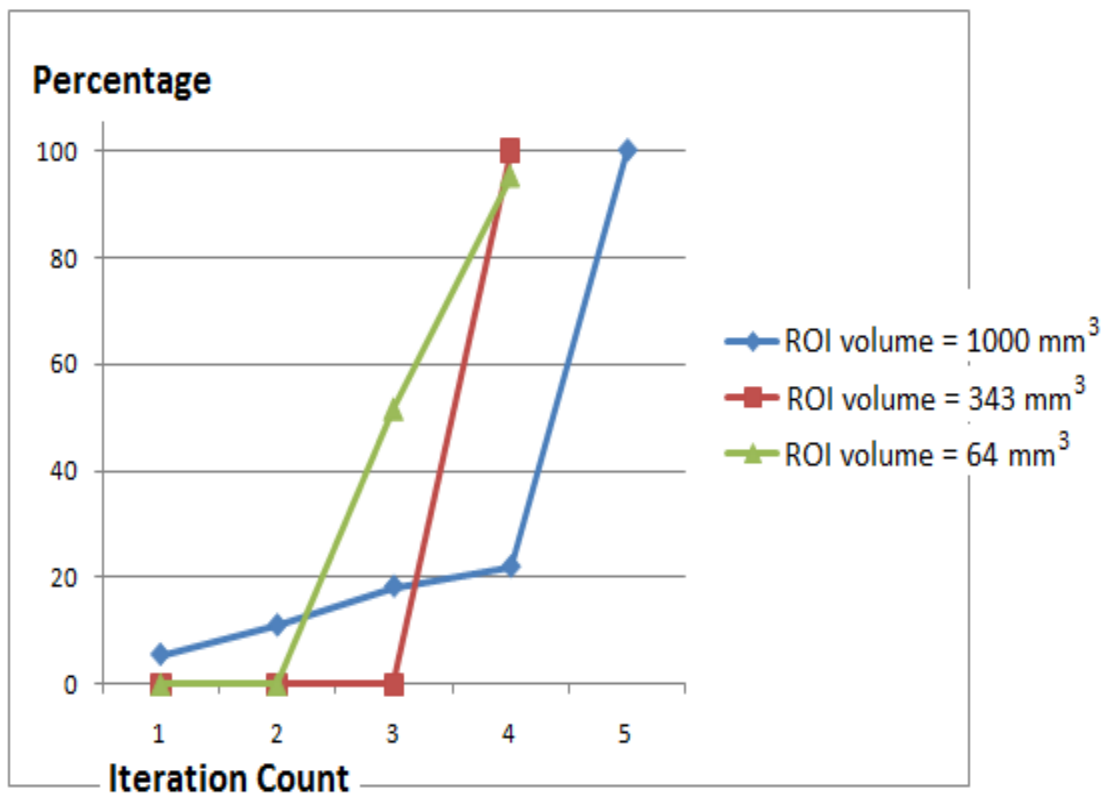
Figure 4.13 Graph of percentage versus iteration count. The figure shows the data for three regions of interests (ROIs) of different volumes. It is seen that the algorithm converges quickly for smaller regions as compared to the larger regions. Thus larger regions consume more computation time [a * (n + 1) time units] as compared to the smaller regions [a * n time units] as it requires more iterations. Here a*n is the computation time for n number of iterations each running for time = a units. Thus the computation time increased only fractionally (n + 1) minutely with an increase in the volume of the ROI.

Thus we can be conclude that a larger region of interest can be used at a minor cost of computation time so as to converge over a larger area and to effectively extract the absorption coefficient within the ROI. However the capability of the graphics card o handle large amounts of memory also limits the increase in the region of interest. In this study the Nvidia card GTX 580 was used. It could support an ROI of 1000mm3 due to the limitations of the shared and global memories of the card. However large ROIs could

be simulated by mapping the recovered absorption coefficients to a fixed set of values as determined by the global and shared memory limitations of the card. This method could be effective in increasing the ROI for convergence and would use less computation power. However such a method could introduce an error while assigning approximate values for absorption coefficients.

4.3.5 <u>Change in Number of Photons</u>

The efficiency of the iteration routine also depends on the number of photons simulated. More the number of photons, greater is the optical resolution. A smoother fluence profile decreases the systemic error. In this study, the simulation was done using different photon numbers to study its effect on fluence and energy profiles and its effectiveness in iterative recovery of the absorption coefficient. Three photon sizes (1000, 10000 and 50000) were generated and its effects on fluence profiles were studied. Figure 4.14 (a - c) shows the normalized fluence profiles through the object centers around the object.

The fluence curve becomes smoother with an increase in the number of photons. A larger number of photons increases the fluence which in turn helps creates smoother transition of energy change between voxels. This helps in more accurate prediction of optical properties of the object simulated. However an increase in the number of photons also increases the computation time. The parallel multithreading capability of the Nvidia graphics card could be used to reduce the computation time by using more number of threads while increasing the number of simulated photons.

The need for more photons to be simulated also reinforces the belief that sufficient illumination is required in real life imaging systems in order to acquire more information within an image. The need for more number of photons also requires graphic cards capable of handling more number of multithreading tasks. In this study a maximum of 100000 photons (per launch) have been simulated, without significantly increasing the

computation time and by using the multithreading capability of Nvidia graphics cards. However the limit is reached when the global and shared memories of the graphics card can no longer support the simulation.
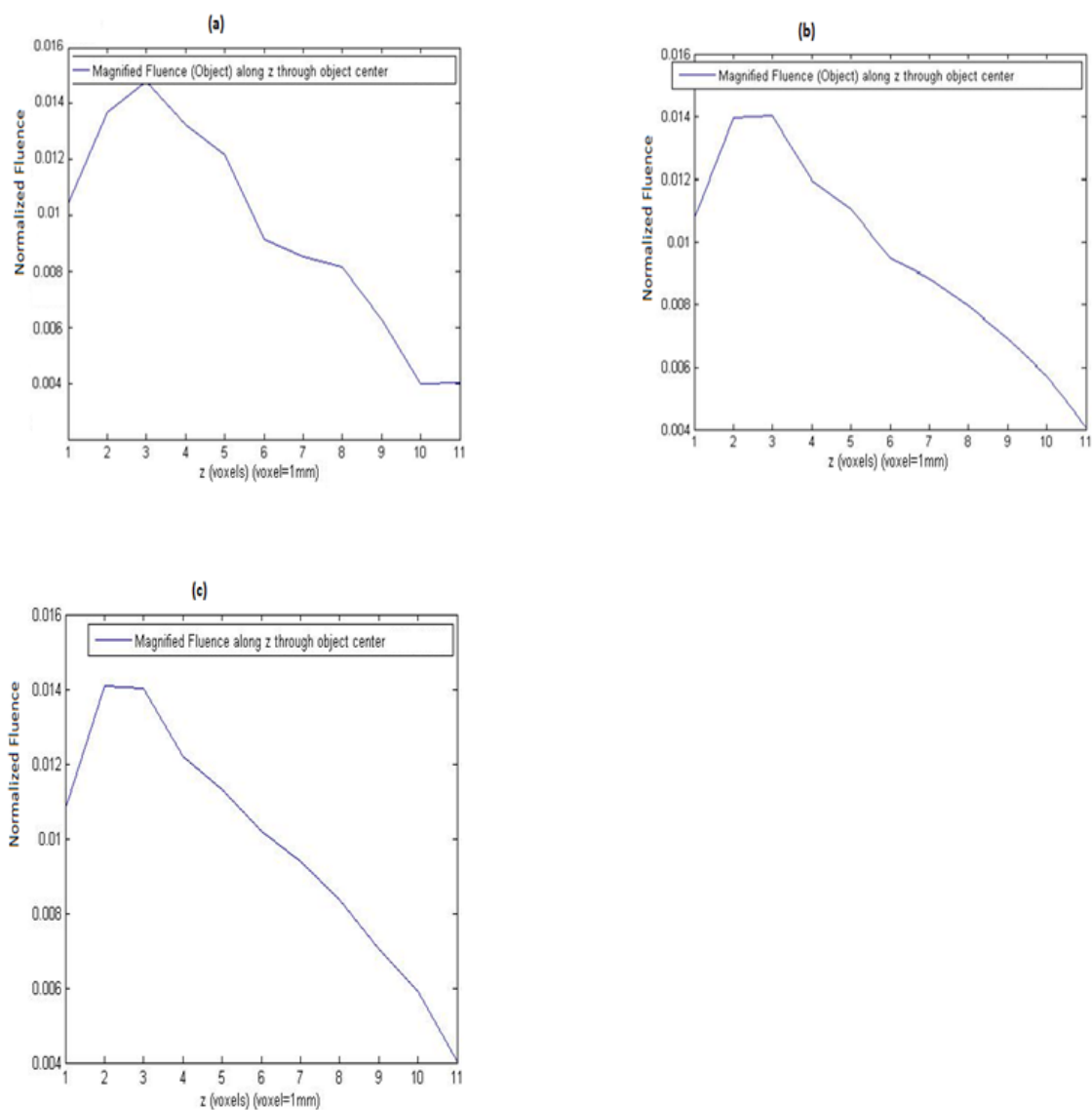
Figure 4.14 Magnified fluence through object center for (a) 1000 photons, (b) 10000 photons, and (c) 50000 photons

5. FLUENCE STUDIES FOR INTEGRATION WITH PCT SCANNER

In order to successfully validate the iterative Monte Carlo code which was developed to improvise the image reconstruction with the PCT scanner, we need to be able to measure the fluence, generated by the propagation of the laser beam, at different points inside the tissues. The current studies which have been used so far for this purpose are thermal calorimetric measurements using a calorimeter and electric measurements using a photodiode. However these techniques cannot be used to measure the fluence inside a mouse within the PCT scanner, as they depend on the orientation of the detector to the incident light beam. Hence, for our purpose we need an isotropic detector which absorbs/detects photons equally in all directions and is easily incorporated within tissues during PCT scans. Hence, an optical fiber with a spherical tip attached to it was designed and calibrated. The design was based on the idea proposed by Michael Shaffer from Dr Stanz' laboratory and was calibrated to measure isotropic absorption of light photons. Although the dosimetry measurements using tissue phantoms could not be made in this study, the angular response of these probes was studied to determine its isotropic nature and to obtain the best possible design.

5.1 Design of Fluence Probe

The probe is designed such that the photons collected by the imaging tip to be able to enter the optical fiber. The spherical nature of the tip helps in collecting photons equally in all directions, while the highly scattering material used in preparing the tip needs ensures that light undergoes multiple scattering events before entering the fiber tip. This ensures a uniform isotropic response which is independent of the incident angle of the light beam[23, 24]. Along with my colleague and mentor Michael Schaffer, we were able

to produce two types of probes using highly scattering materials such as Titanium dioxide and Nylon. The fractional volumes of the material used (TiO_2 or Nylon) for the probe tip determines the number of scattering events per unit length, and thus the scattering coefficient[23, 24].

The fiber optic correction factor (Fc) needs to be applied in order to take into account the portion of the solid angle which is blocked due to introduction of the fiber optic tip[23, 24]. This is given by:

$$F_c = \frac{\Omega_{sphere}}{\Omega_{sphere} - \Omega_{cable}}$$

(31)

$$F_c = \frac{4\pi}{4\pi - 2\pi \int_0^{\arcsin(\frac{d}{D})} \sin\theta d\theta}$$

(32)

Substituting in the limits of integration and simplifying:

$$F_c = \frac{2}{1 + \cos[\arcsin(\frac{d}{D})]}$$

(33)

Here d and D are the diameters of the fiber and probe respectively. The Table 5.1 shows the effect of the sphere diameter on Fc:

Table 5.1 Relative cable gain due to blind spot on sphere

Fiber Diameter (mm)	Sphere Diameter (mm)	Fc
0.4	0.8	1.0718
0.4	1.2	1.0294
0.4	1.5	1.0184
0.4	2	1.0102
0.4	2.5	1.0065

The following mold in Figure 5.1 (designed and machined by Michael Shaffer, Exacto Machine and Tool Inc., Indianapolis, IN) was used to cast the spherical probes:

Figure 5.1 Mould design for casting spherical probes

5.2 Measurement of Angular Response using PIN Photodiode

In order to record the amount of light entering the fiber, the optical cable is connected to a ET-2030PIN photodiode (ET-2030 PIN Electro Optics Technology Inc., Traverse City, MI). The output of the photodiode is connected to a digital oscilloscope (Tektronix TDS3052B), whose output is normalized by the spectral response of the ET-2030 unit. The experimental setup is shown in Figure 5.2.

Figure 5.2 Experimental set up for measuring equatorial and azimuthal angular response of the fluence probes

The photodiode is operated in the Photo Conductive (PC) mode below the breakdown voltage of the diode so as to achieve a greater linear range for change in photon fluence, at the expense of generating more dark current. The peak voltage of the diode is measured by coupling the photodiode to the oscilloscope using a 50 ohm impedance setting, while sampling is done with pulsed Q-switched signal as trigger to adjust timing delay.

5.3 Probe Calibration

In the current study the probe will be calibrated against a wavelength of 696 nm which is the wavelength of light used to perform tumor imaging studies. This is done by measuring the output peak voltage across various equatorial and azimuthal angles. A stepper motor is used to rotate the probe around its axis for equatorial measurements while the azimuthal angle is changed by manually adjusting the probe axis with respect to the light beam. The equatorial angles range from 0 to 360 degrees in steps of 15 degrees while the azimuthal angles are changed in steps of 10 degrees from 0 to 150 degrees. The physical limitations such as the scanner dimensions and the probe dimensions prevented us from taking the entire azimuthal range of 180 degrees. The PCT LOM is then used to take measurements of the beam output power at each data point and is used to normalize the photodiode output.

5.4 Summary of Angular Responses

Based on the concentration of titanium dioxide or nylon, the following graph was plotted of the diffusion coefficient versus concentration in Figure 5.3. The equatorial uniformity of the nylon and titanium probes is shown in Figure 5.4 while the azimuthal response is shown in Figure 5.5.
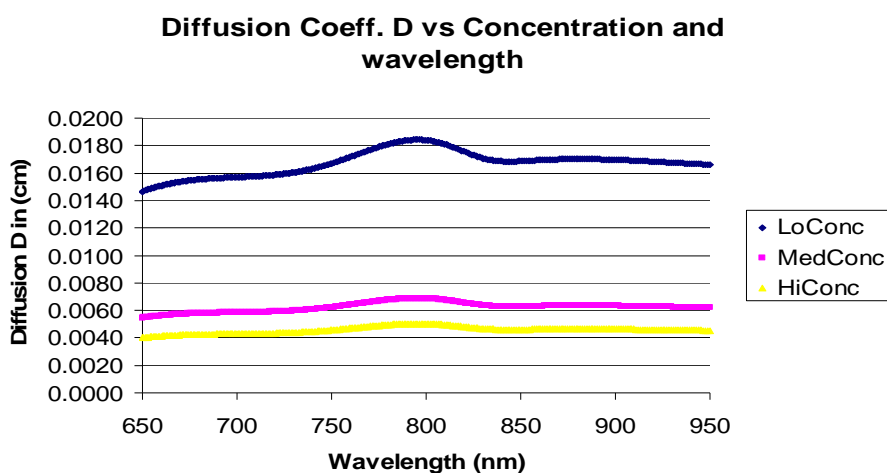
Figure 5.3 Plot of diffusion coefficient versus wavelength
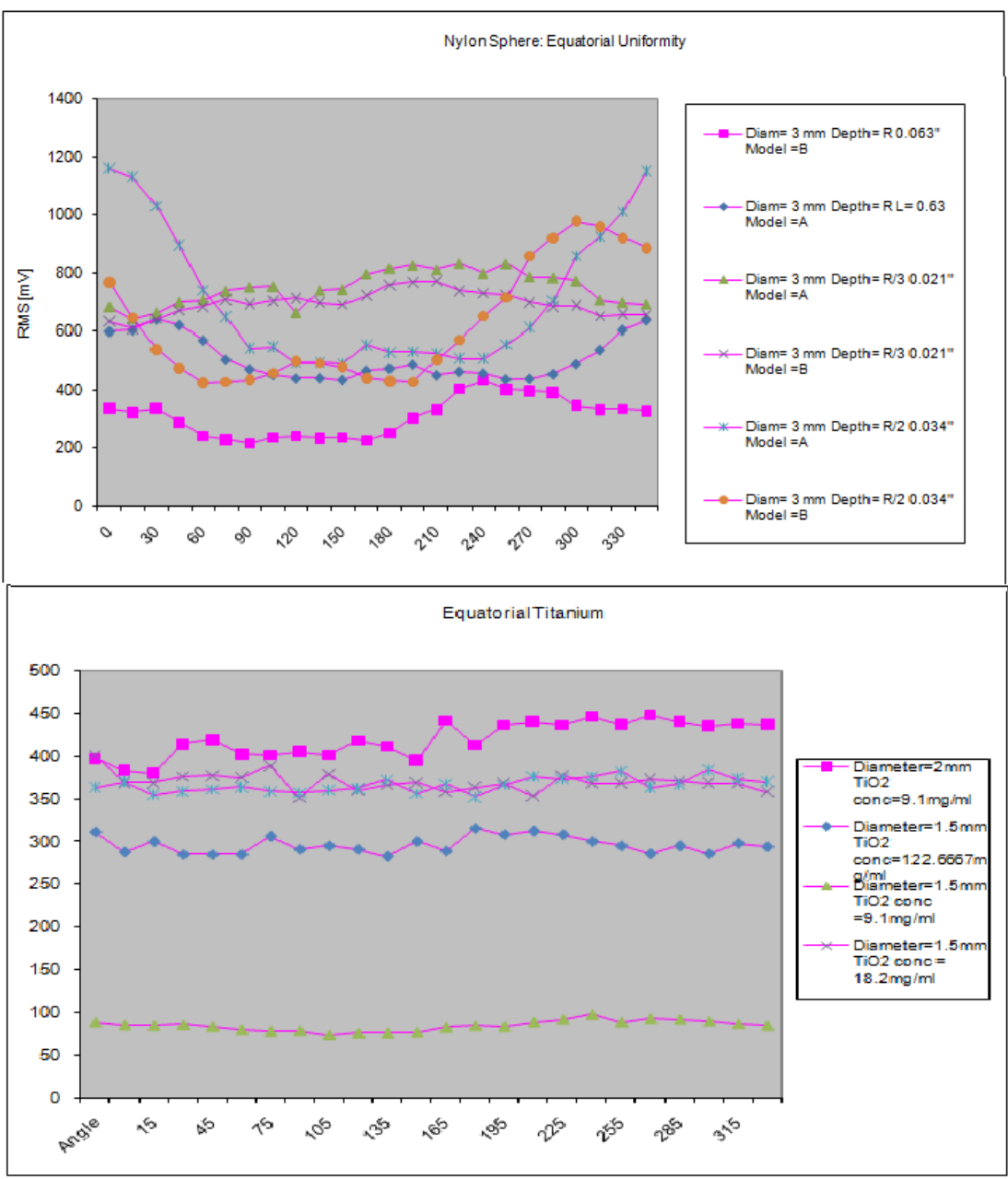
Figure 5.4 Equatorial response of Nylon and Titanium spheres. The equatorial response of the titanium probes is more uniform as compared to nylon probes
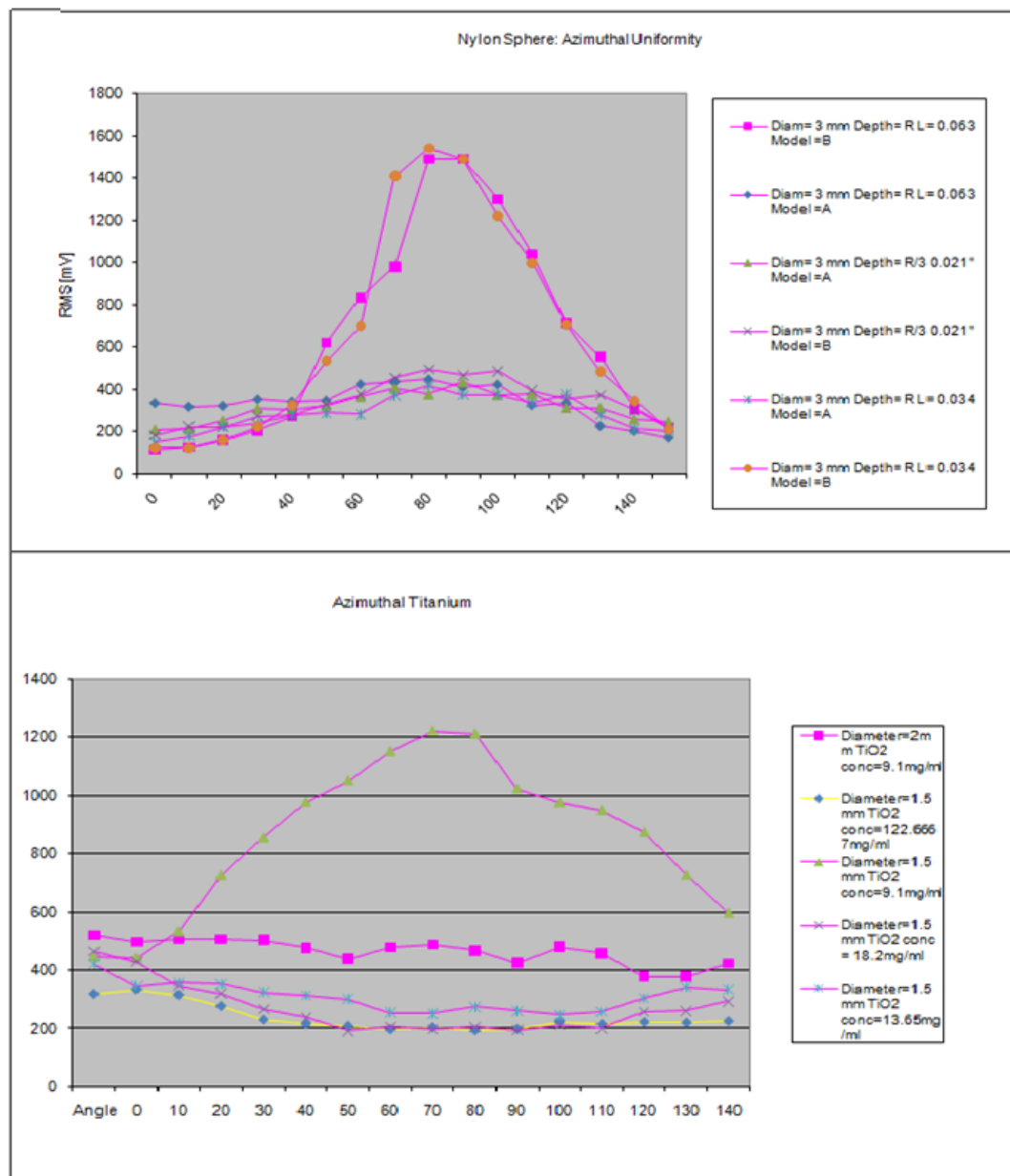
Figure 5.5 Azimuthal response of Nylon and Titanium spheres. The equatorial response of the titanium probes is more uniform as compared to nylon probes

The equatorial and azimuthal responses of the probes varies with probe concentration, diameter and the depth of penetration of the optical fiber within the probe sphere. Overall the equatorial and azimuthal responses of the titanium sphere are more

uniform as compared to nylon spheres. However in order to justify this observation, statistical analysis was performed to measure the standard deviation of the probe responses. The variation was measured by calculating the ratio of the standard deviation to the average values of the normalized rms values. The standard deviation plots are shown in Figure 5.6 while the plots showing variation of the angular responses is shown in Figure 5.7.
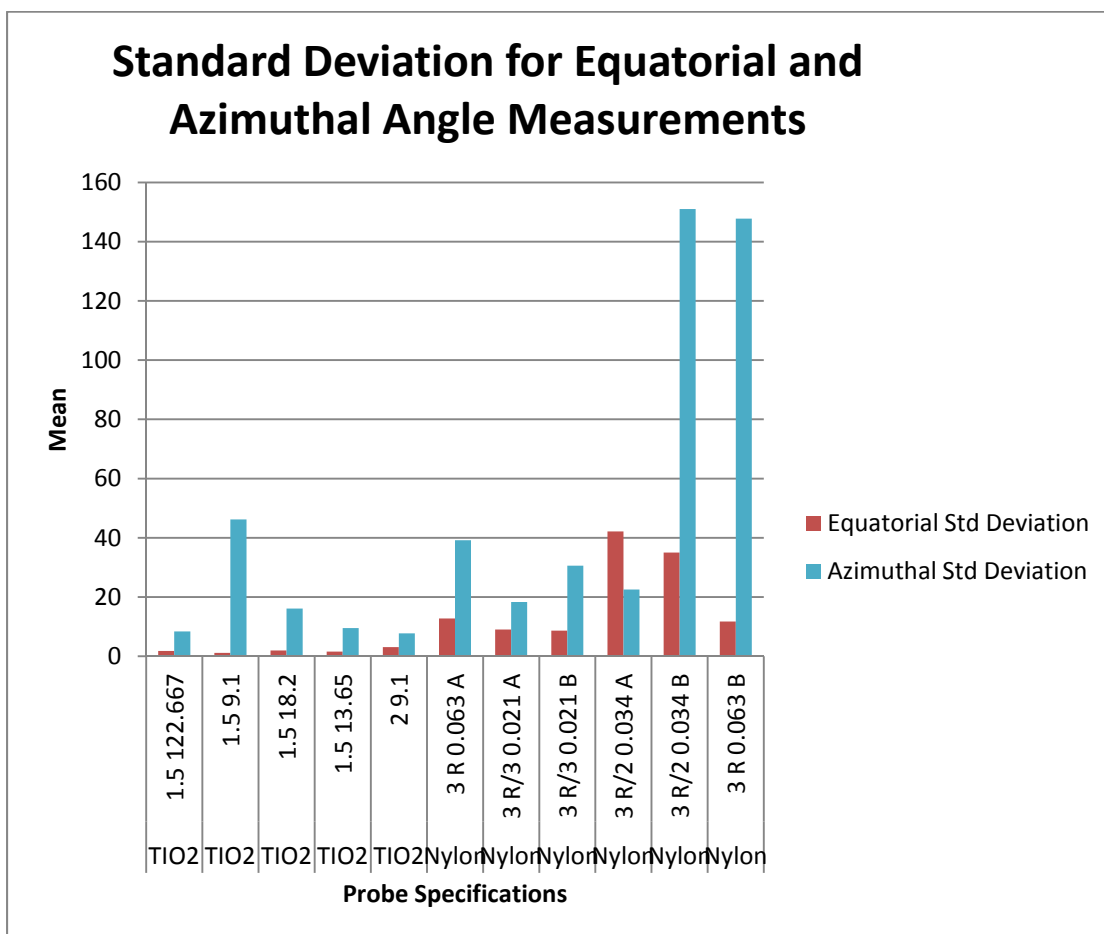
Figure 5.6 Standard deviation plots for equatorial and azimuthal responses of Titanium and Nylon probes. Titanium probes show more uniform response as compared to the Nylon probes
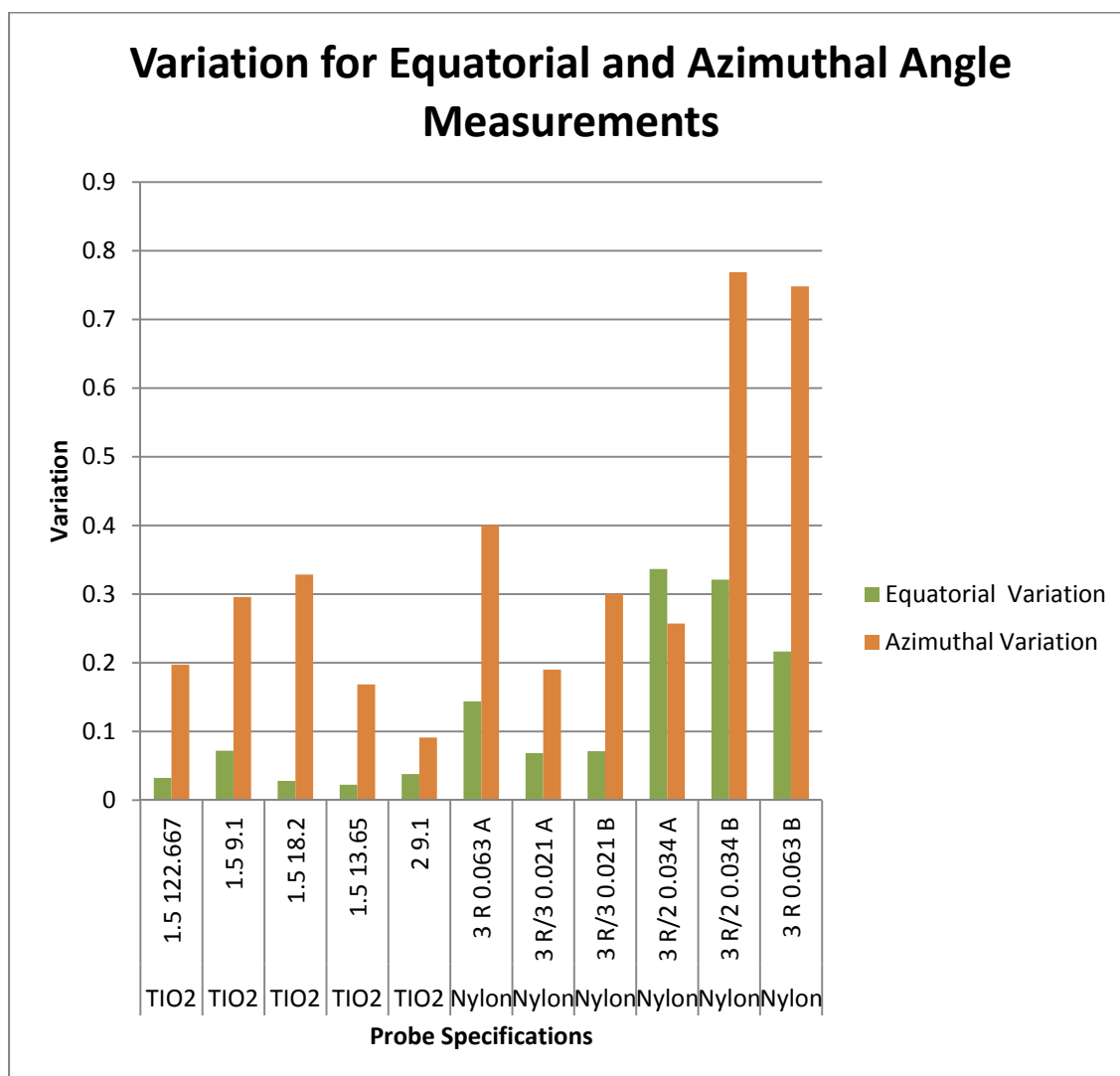
Figure 5.7 Equatorial and Azimuthal variations of Titanium and Nylon probes. Titanium probes show less variation as compared to the Nylon probes

The variation and standard deviation plots in Figures 5.6 and 5.7 were used to determine the best possible probe combinations. Since titanium probes showed a more uniform response, two such probes were identified and compared, namely the probes with 1.5 mm and 2 mm diameters. These were made with 5 mg/ml concentration of titanium dioxide. The plots of equatorial and azimuthal variation is plotted in Figure 5.8.
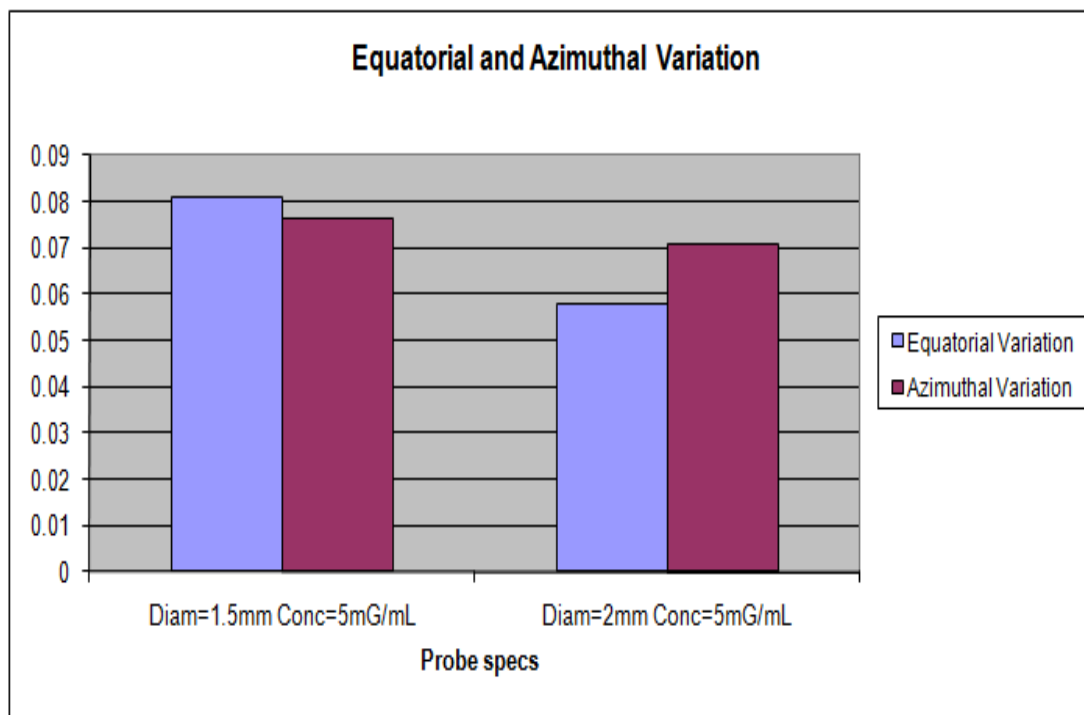
Figure 5.8 Equatorial and Azimuthal variation of titanium probes with 1.5 mm and 2 mm diameters

From Figure 5.8, it is seen that the equatorial and azimuthal variation of the probe with 2 mm diameter is less compared to the probe with 1.5 mm diameter. This is due to the fact that larger diameter allows a more uniform distribution of fluence within the sphere.

The Table 5.2 shows the final summary of the probe responses. The responses have been graded manually into 3 categories, namely good, fair and bad. A good response is one which has low values of standard deviation and variation in both the azimuthal and equatorial response, while a bad response shows higher values. A fair response indicates a grade between good and bad. The results from these analysis shows that titanium probes having a diameter of 1.5 mm show a uniform response and is recommended for further calibration and tissue fluence studies.

Table 5.2 Summary of angular response of Titanium and Nylon probes

Type	Specs	Equatorial Uniformity	Azimuthal Uniformity
TIO2	1.5 122.667	Good	Fair
TIO2	1.5 9.1	Fair	Poor
TIO2	1.5 18.2	Good	Fair
TIO2	1.5 13.65	Fair	Good
TIO2	2 9.1	Good	Good
Nylon	3 R 0.063 A	Fair	Fair
Nylon	3 R/3 0.021 A	Fair	Fair
Nylon	3 R/3 0.021 B	Fair	Fair
Nylon	3 R/2 0.034 A	Bad	Fair
Nylon	3 R/2 0.034 B	Bad	Bad
Nylon	3 R 0.063 B	Fair	Bad

Thus optical dosimetry probes could be potentially used to determine the fluence and energy distributions within tissues. The data obtained via these probes can be used to calibrate the PCT scanner and used to obtain the energy profiles, which could in turn be used as reference energy maps to extract the optical coefficients within tissues of complex geometry using the iterative routine. While this being a pilot study, further studies need to be performed to determine the energy profiles of these probes with respect to the laser output power.

6.   CONCLUSION AND FUTURE WORK

This study has been a continuation of the work done by Dr Stantz and Jye Cheong in developing an effective method to quantify the photoacoustic effect in tissues which show high rate of opto-acoustic conversion properties. The role of the absorption coefficient in this conversion process has been studied at a molecular scale. The uniqueness of this study lies in its ability to extract and recover the absorption properties of the imaged object on a voxel by voxel basis in a 3 dimensional medium. Thus its inherent ability to be integrated with the PCT scanner makes it a unique technique for calibrating the scanner. This study however needs to be integrated with sufficient data obtained through fluence studies in tissues using the dosimetry probes. The need to obtain the photoacoustic coefficient of conversion is the main focus of this study. Thus further research needs to be conducted to study the process of conversion of light fluence into thermo elastic expansion and subsequently the generation of the acoustic wave. This requires the study of the thermal and elastic properties of the molecules and their dependence on the light distribution within the tissues. The PCT scanner output could be used to determine this property through the use of the back projection algorithm to obtain the reference energy profile. Once integrated with the PCT images, the iterative recovery method using Monte Carlo could form a powerful diagnostic tool to determine the optical and acoustic properties of the imaged tissues. This would help in the diagnosis of cancer and other ailments.

This entire study was divided into several steps. The first part of the study looked at the best possible way to implement multithreading and parallel processing so as to

reduce the computational speed. This was done by making use of the basic Monte Carlo code as developed by Dr Fang and modifying it to suit the imaging environment in a photoacoustic scanner. The second part dealt with simulations which were performed to study the performance of the Monte Carlo algorithm so as to determine its efficacy and accuracy in a photoacoustic environment. Finally the iteration algorithm was developed and implemented so as to extract the absorption coefficient from the simulated object by iterative recovery method. In all these studies the Monte Carlo code was found to perform satisfactorily and was validated with the help of the iteration method.

Simulations were performed with known optical properties (referred in previous studies) so as to recover the absorption coefficient through the iterative method. The effects of the photon numbers, change in regions of interest, as well as use of different values of optical coefficients was studied. The iterative routine was able to converge within 4-6 iterations and hence, was found to be effective in time and efficiency to recover the optical properties of the tissue. The fluence studies performed using the isometric probes were successful in producing a isotropic response and hence, hold a promise to be used to determine the fluence within tissues in a real imaging system.

Future work in this research has to involve fluence based studies to determine the energy distribution in tissues and to validate it with the Monte Carlo software. A part of this work has already been done with the design of isotropic fluence probe to study tissue illumination. Such isotropic probes can be used to determine fluence within tissue samples as well as optical phantoms so as to study the distribution of light energy and thus could be used to determine the optical properties of the tissues. These properties could act as the preliminary inputs to the Monte Carlo software. However in order to validate the PCT scanner, we will have to determine the energy distribution using back projection algorithm as used in the scanner and thus a reference energy map can be obtained. Furthermore, such a map serves as a reference map to compare the Monte Carlo output with the PCT output and o determine the accuracy of the iteration algorithm. Thus the absorption coefficient can be determined based on these two inputs (fluence and

energy maps). The same iterative method can also be used to determine the other optical properties by using sufficient details of the other optical parameters.

More work needs to be done in areas of understanding the acoustic conversion from absorbed photon energy and to determine the relationship between the light energy and acoustic energy due to the volumetric expansion. Use of optical and acoustic phantoms would help in order to quantify this relationship. Tissues have complex structures and boundaries and hence, the optical properties vary depending on the geometry, type and depth of the tissues. These details need to be represented within optical phantoms so as to get more real life structures which could be imaged and validated using Monte Carlo techniques. This work is currently in process at Dr Stantz's research laboratory.

LIST OF REFERENCES

LIST OF REFERENCES

[1]   W. Cheong, S. A. Prahl, and A. Welch, "A review of the optical properties of biological tissues," in *IEEE journal of quantum electronics*, vol. 26, pp. 2166–2185, 1990

[2]   W. M. Star, "Comparing the P3-approximation with diffusion theory and with Monte Carlo calculations of light propagation in a slab geometry," in *SPIE Proceedings on Dosimetry of Laser Radiation in Medicine and Biology*, vol. IS5, pp. 146- 154, 1989.

[3]   S. A. Prahl, *Light transport in tissue*, Ph.D. Dissertation, University of Texas at Austin, 1988.

[4]   L. O. Svaasand, D. R. Doiron, and A. E. Profio, "Light distribution in tissue during photoradiation therapy," in *Workshop on Porphyrin Sensitization*, 1981.

[5]   G. Yoon, S. A. Prahl and A. J. Welch, "Accuracies of the Diffusion Approximation and its Similarity Relations for Laser Irradiated Biological Media," in *Applied Optics*, vol. 28, pp. 2250-2255, 1989.

[6]   A. Ishimaru, *Wave Propagarion and Scattering in Random Media*, 2nd ed., Wiley-IEEE, vol. 12, 1999.

[7]   S. L. Jacques and S. A. Prahl, "Modeling optical and thermal distributions in tissue during laser irradiation," in *Lasers Surg. Med.*, vol. 6, pp. 494-503, 1987.

[8]   M. J. C. Gemert, A. J. Welch, W. M. Star, M. Motamedi, and W. F. Cheong, "Tissue ptics for a slab geometry in the diffusion approximation," in *Lasers Med. Sci.*, vol. 2, pp. 295-302, 1987.

[9]   H. C. Hulst, *Multiple Light Scattering*, New York: Academic, vol. 2, 1980.

[10]   G. Yoon, S. A. Prahl, and A. J. Welch, "Accuracies of the diffusion approximation and its similarity relations for laser irradiated biological media,'' in *Appl. Opt.*, vol. 28, pp. 2250-2255, 1989.

[11]   S. A. Prahl, M. Keijzer and S. L. Jacques, "Absorption and flux distributions of light in tissue", in *Med. Phys.,* vol. 10, pp. 824-830, 1983.

[12]   L. Wang, S. L. Jacques, and L. Zheng, "Monte Carlo modeling of light transport in multilayered tissues," in *Computer Methods and Programs in Biomedicine*, vol. 47, pp. 131-146, 1995.

[13]   I. Lux and L. Koblinger, *Monte Carlo Particle Transport Methods: Neutron and Photon Calculation*, CRC Press, vol. 102, 1991.

[14]   J. Cheong, *Monte Carlo simulation for light propagation through tissues*, Master's Thesis, Department of Biomedical Engineering, Purdue University, 2009.

[15]   B. T. Cox, S. R. Arridge, K. P. Köstli, and P. C. Beard, "Two-dimensional quantitative photoacoustic image reconstruction of absorption distributions in scattering media by use of a simple iterative method," in *Applied Optics*, vol. 45, pp. 1866-1875, 2006.

[16]   Q. Fang and D. A. Boas, "Monte Carlo simulation of photon migration in 3D turbid media accelerated by graphics processing units," in *Opt. Express*, vol. 17, pp. 20178-20190, 2009.

[17]   N. Ren, J. Liang, X. Qu, J. Li, B. Lu, and J. Tian, "GPU-based Monte Carlo simulation for light propagation in complex heterogeneous tissues," in *Opt. Express*, vol. 18, pp. 6811-6823, 2010.

[18]   E. Alerstam, T. Svensson, and S. Andersson-Engels, "Parallel computing with graphics processing units for high-speed Monte Carlo simulation of photon migration," in *Biomed. Opt.*, vol. 13, pp. 060504, 2008.

[19]   E. D. Cashwell and C. J. Everett, *A Practical Manual on the Monte Carlo Method for Random Walk Problems*, New York: Pergamon Press, 1959.

[20]   M. H. Kalos and P. A. Whitlock, *Monte Carlo Methods*, John Wiley & Sons, Inc., 1986.

[21]   D. A. Boas, J. P. Culver, J. J. Stott, and A. K. Dunn, "Three dimensional Monte Carlo code for photon migration through complex heterogeneous media including the adult human head," in *Opt. Express*, vol. 10, pp. 159–170, 2002.

[22]   H. Kahn and T. E. Harris, "Estimation of Particle Transmission by Random Sampling Monte Carlo Method", in *National Bureau of Standards Applied Mathematics Series*, vol. 12, U.S. Government Printing Office, 1951.

[23] J. P. Marijnissen and W. M. Star, "Calibration of isotropic light dosimetry probes based on scattering bulbs in clear media," in *Phys. Med. Biol.*, vol. 41, pp. 1191-1208, 1996.

[24] L. Lilge, T. Haw and B. C. Wilson, "Miniature isotropic optial fibre probes for quantitative light dosimetry in tissue," in *Phys. Med. Biol.*, vol. 38, pp. 215-230, 1993.